INTERNATIONAL JOURNAL FOR NUMERICAL METHODS IN FLUIDS
Int. J. Numer. Meth. Fluids 2008; **58**:969–1007
Published online 17 March 2008 in Wiley InterScience (www.interscience.wiley.com). DOI: 10.1002/fld.1779

Surrogate model-based strategy for cryogenic cavitation model validation and sensitivity evaluation

Tushar Goel[1,‡], Siddharth Thakur[1,§], Raphael T. Haftka[1,¶], Wei Shyy[2,*,†,‖] and Jinhui Zhao[2]

[1]*Department of Mechanical and Aerospace Engineering, University of Florida, Gainesville, FL 32611, U.S.A.*
[2]*Department of Aerospace Engineering, University of Michigan, Ann Arbor, MI 48109, U.S.A.*

SUMMARY

The study of cavitation dynamics in cryogenic environment has critical implications for the performance and safety of liquid rocket engines, but there is no established method to estimate cavitation-induced loads. To help develop such a computational capability, we employ a multiple-surrogate model-based approach to aid in the model validation and calibration process of a transport-based, homogeneous cryogenic cavitation model. We assess the role of empirical parameters in the cavitation model and uncertainties in material properties via global sensitivity analysis coupled with multiple surrogates including polynomial response surface, radial basis neural network, kriging, and a predicted residual sum of squares-based weighted average surrogate model. The global sensitivity analysis results indicate that the performance of cavitation model is more sensitive to the changes in model parameters than to uncertainties in material properties. Although the impact of uncertainty in temperature-dependent vapor pressure on the predictions seems significant, uncertainty in latent heat influences only temperature field. The influence of wall heat transfer on pressure load is insignificant. We find that slower onset of vapor condensation leads to deviation of the predictions from the experiments. The recalibrated model parameters rectify the importance of evaporation source terms, resulting in significant improvements in pressure predictions. The model parameters need to be adjusted for different fluids, but for a given fluid, they help capture the essential fluid physics with different geometry and operating conditions. Copyright © 2008 John Wiley & Sons, Ltd.

Received 15 February 2007; Revised 31 December 2007; Accepted 2 January 2008

KEY WORDS: cavitation; code validation; cryogenics; multiple surrogates; global sensitivity analysis

*Correspondence to: Wei Shyy, Department of Aerospace Engineering, University of Michigan, Ann Arbor, MI 48109, U.S.A.
†E-mail: weishyy@umich.edu
‡Currently with Livermore Software Technology Corporation, Livermore, CA, U.S.A.
§Visiting Professor.
¶Distinguished Professor.
‖Clarence L. 'Kelly' Johnson Professor.

Contract/grant sponsor: Institute for Future Space Transport
Contract/grant sponsor: National Science Foundation; contract/grant number: 0423280

1. INTRODUCTION

Code validation and verification are complex and time consuming but essential exercises to ensure the accuracy of the predictions of computational fluid dynamics (CFD) codes [1–6]. For computational verification and validation exercises, multiple aspects need to be addressed. One needs to ensure that the numerical representation of the analytical model approaches the correct solution as the grids and time-step sizes approach the limiting values; this is the so-called verification. Verification deals with programming errors, algorithmic insufficiencies and inconsistencies. The second aspect is to investigate whether and how a particular physical model can reproduce or, at least, satisfactorily approximate the observed phenomena and reproduce the experimental measurements. That is, one should examine the propriety of the mathematical models and assumptions; this is the so-called validation.

Code validation or model validation is further complicated when the mathematical model involves adjustable parameters because there is a danger of fitting the experimental errors rather than the physical reality. We demonstrate for cryogenic cavitation how the tools of surrogate modeling and global sensitivity analysis (GSA), which are extensively used in design and optimization of computationally expensive problems [7, 8], can help with model validation and calibration.

1.1. Cavitating flows: significance and previous computational efforts

Cavitation is one of the foremost problems observed in the turbomachinery such as inducers, pumps, turbines, marine propellers, nozzles, hydrofoils, etc. due to wide ranging pressure variations in the flow. Cavitation occurs when the local pressure in the flow falls below the vapor pressure and, consequently, the fluid undergoes a phase change [9–11]. Cavitation induces noise, mechanical vibrations, material erosion and can severely impact the performance as well as the structural integrity of fluid machinery. The study of cavitating flows is complicated by simultaneous presence of turbulence, multiple time scales, large density variations or phase change, interfacial dynamics, etc. Owing to its practical importance and rich physics, cavitating flow is a topic of substantial interest and challenge to the computational community.

The study of cavitating flows in cryogenic environment has practical importance for space applications because cryogens often serve as fuels for space launch vehicles [12]. A key design issue related to such liquid rocket fuel and oxidizer pumps is the minimum pressure that the design can tolerate for a given inlet temperature and rotating speed. At low inlet pressure (to reduce tank weight) and high pump rotational speeds (to reduce engine weight), cavitation is prone to appear in the inducer section. To date, there is no established method in industry to estimate the actual loads due to cavitation on inducer blades. There have been methods proposed, each with its limits on validity and challenges [13]. Most rocket engine systems designed in the U.S. have experienced issues with cavitating elements in the pump. This includes recent programs such as the alternate turbo pump (ATP) for the space shuttle main engine (SSME), the Fastrac LOX pump, and the RS-68 commercial engine [13]. An integrated framework based on computational modeling and control strategies is desirable to treat this critical and difficult issue. It is clear that the design of efficient turbomachinery components requires understanding and accurate prediction of the cryogenic cavitating flows.

Cavitating flow computations have been conducted using both density-based [14–17] and pressure-based numerical approaches [18–21], with the cavitation models developed based on (i) Rayleigh–Plesset type of bubble formulation [22], which separates the liquid and the vapor regions

DOI: 10.1002/fld

based on the force balance notion, and (ii) homogeneous fluid approach [19], which treats the cavity as a region consisting of continuous mixture of liquid and vapor phases. In the homogeneous fluid model, the density field is commonly modeled via either a generalized equation of state [23, 24] or a transport equation of the liquid/vapor phase fraction [14, 17, 19, 20, 25]. Recent efforts made in computational and modeling aspects of cavitating flows are discussed by Wang *et al.* [26], Senocak and Shyy [20, 21], Ahuja *et al.* [15], Venkateswaran *et al.* [16], Preston *et al.* [27], and Utturkar *et al.* [28].

1.2. Influence of thermal environment on cavitation modeling

To date, the majority of the cavitation modeling efforts have focused on the assumption that cavitation occurs with negligible energy interactions (isothermal condition). This assumption is reasonable for cavitation in non-cryogenic fluids but fails for thermo-sensible fluids such as liquid hydrogen and liquid oxygen (cryogens) due to the differences in material properties (low liquid–vapor density ratio, low thermal conductivities, steep slope of pressure–temperature saturation curves, etc.) and the coupling of thermal effects such as variation in vapor pressure/density with temperature, etc. [25, 28–30]. Figure 1 [31] illustrates the behavior of the physical properties of two representative cryogens, liquid nitrogen and liquid hydrogen, in the liquid–vapor saturation regime. The temperature range in the plots is chosen based on the general operating condition of the fluids, which is close to the critical point. We observe substantial variation in the material properties with changes in the temperatures. Relatively, the variation in the material properties (vapor pressure, liquid–vapor density ratio, latent heat of vaporization, etc.) with temperature for liquid hydrogen is higher than that observed for liquid nitrogen.

As summarized by Utturkar *et al.* [28], dynamic similarity in the case of isothermal cavitation is dictated by the cavitation number σ (Equation (1) with constant vapor pressure p_v). In the context of cryogenic cavitation, the actual cavitation number needs to be defined as follows [10]:

$$\sigma = \frac{p_\infty - p_v(T_c)}{0.5\rho_l U_\infty^2} \tag{1}$$

where p_∞ is the reference pressure, U_∞ is the reference velocity, ρ_l is liquid density, and T_c is the temperature in the cavity. The local cavitation number can be related to the far-field cavitation number (based on the vapor pressure there) by the following first-order approximation [10]:

$$\frac{1}{2}\rho_l U_\infty^2(\sigma - \sigma_\infty) = \frac{\mathrm{d}p_v}{\mathrm{d}T}(T_\infty - T_c) \tag{2}$$

Equation (2) clearly indicates that the cumulative effect of the aforesaid factors would produce a notable rise in the local cavitation number and subsequently suppress the intensity of cavitation. Representative values of the vapor pressure gradients ($\mathrm{d}p_v/\mathrm{d}T$) in the operating temperature regime for liquid nitrogen and hydrogen are 20 and 37 kPa/K, respectively.

The influence of thermal effects on cavitation has been numerically and experimentally investigated as early as 1956. Stahl and Stepanoff [32] introduced a 'B-factor' method to estimate temperature drop in terms of the ratio of the vapor volume to liquid volume during vaporization process and used it to appraise head depression due to thermodynamic effects in cryogenic cavitation. Gelder *et al.* [33], Ruggeri and Moore [34], and Hord [35] simplified and extended this B-factor theory to account for dynamic effects via bubble growth, varying cavity thickness, and convective heat transfer. Holl *et al.* [36] presented an entrainment theory to correlate the

DOI: 10.1002/fld

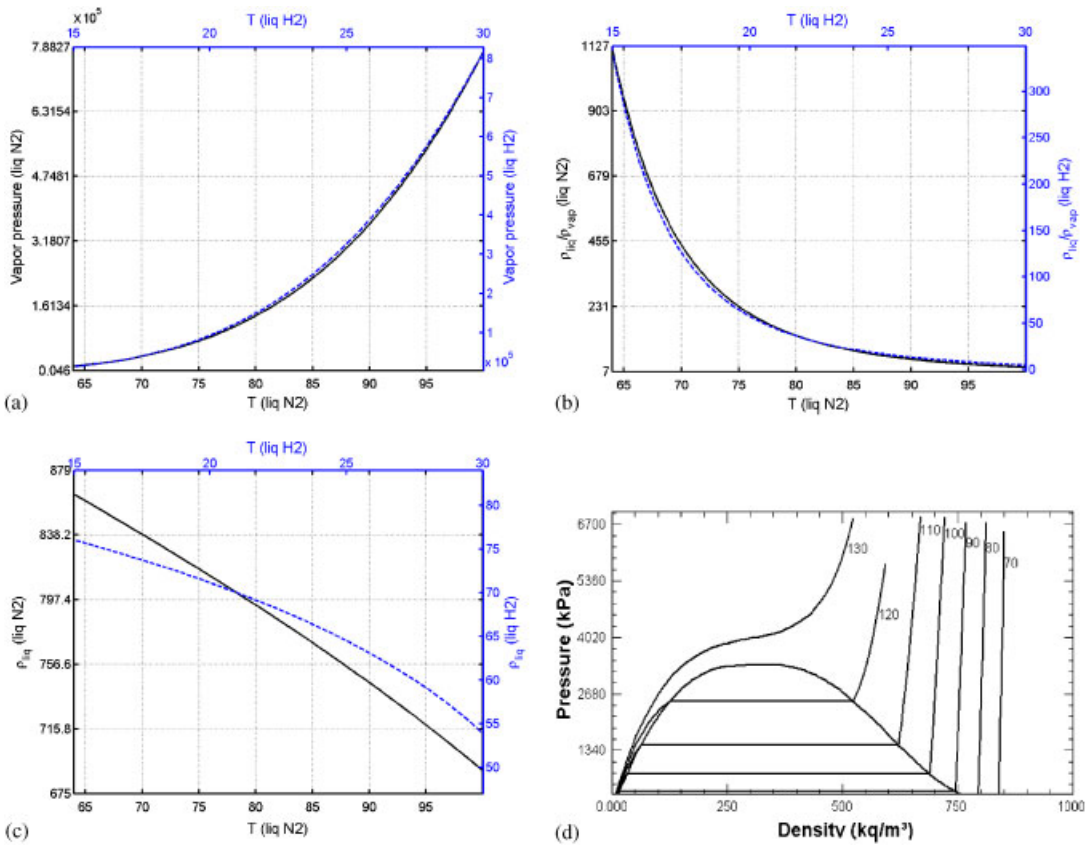

Figure 1. Variation of physical properties for liquid nitrogen [31] (solid line, relevant x-axis is on bottom and y-axis is on left) and liquid hydrogen [31] (dashed line, relevant x-axis is on top and y-axis is on right): (a) vapor pressure *versus* temperature along saturation line; (b) ratio of liquid density to vapor density *versus* temperature along saturation line; (c) liquid density *versus* temperature along saturation line; and (d) pressure–density chart—lines denote isotherms (liquid N_2).

temperature depression and flow parameters. Cooper [37] used a non-dimensional vaporization parameter along with a baratropic equation of state to incorporate pressure depression due to thermal effects while numerically simulating liquid hydrogen pumps. Brennen [10, 11] and Franc *et al.* [38] presented methods of assessing thermodynamic effects on bubble dynamics by incorporating it into Rayleigh–Plesset equation. We refer the reader to the works by Hosangadi and Ahuja [30] and Utturkar [29] for more insight into the application regime and the pros and cons of these methods.

1.3. Experimental and numerical modeling of cryogenic cavitation

Hord [35, 39] conducted by far the most comprehensive experiments on cryogenic cavitation with liquid nitrogen and hydrogen, under different sets of inlet velocity and temperature conditions, and employing a variety of geometries (hydrofoil and ogives of varying diameters). Temperature and pressure data in the cavitating region, which have been commonly employed for numerical

DOI: 10.1002/fld

validation [40], were acquired over the geometries at regular spatial intervals by thermocouples and pressure sensors.

There have been limited computational studies for cryogenic cavitating flows. The key challenges for numerical computations are the presence of strong non-linearity in the energy equation and the temperature dependence of physical properties [31] such as vapor pressure and density ratio (as seen from Figure 1(a) and (b)). The main features of a few selected numerical studies [25, 40–49] are summarized in Table I.

A transport-based cavitation model, proposed by Merkle *et al.* [14], has been adopted in multiple efforts for non-cryogenic conditions. The same basic framework can also be used to simulate cryogenic cavitating flows, subject to proper modification of the model parameters to better reflect the transport properties of cryogenic fluids and physical mechanisms of the flow environment. Utturkar *et al.* [25] showed that the accuracy of predictions is affected by the model parameters and there is a need to calibrate the model parameters to account for cavitation in cryogenic conditions. As discussed earlier, the temperature-dependent material properties also play a significant role in the

Table I. Summary of a few relevant numerical studies on cryogenic cavitation.

Reference	Main features
Reboud *et al.* [41]	(a) Potential flow equations with semi-empirical formulation
Delannoy and Reboud [42]	(b) Simplistic interfacial heat transfer equation (suitable only for sheet cavitation)
	(c) Energy equation not solved
Deshpande *et al.* [43]	(a) Explicit interface tracking
	(b) Simplistic model for vapor flow inside cavity (suitable only for sheet cavitation)
	(c) Energy equation solved only in the liquid region
Lertnuwat *et al.* [44]	(a) Incorporated energy balance in Rayleigh–Plesset equation to model bubble oscillations
	(b) Good agreement with DNS but deviations under isothermal and adiabatic conditions
Tokumasu *et al.* [45, 46]	(a) Explicit interface tracking
	(b) Improved model for vapor flow inside the cavity (suitable only for sheet cavitation)
	(c) Energy equation solved only in the liquid region
Hosangadi and Ahuja [40]	(a) Solved energy equation in the entire domain with dynamic update of material properties
Hosangadi *et al.* [47]	(b) Some inconsistency with experimental results is noted
	(c) Noticed significant changes in the cavitation model parameters in cryogenic and non-cryogenic conditions
Rachid [48]	(a) Theoretical model to account for compressibility effects in a liquid–vapor mixture
	(b) Introduced dissipative effects in intermediate phase transformation between two extreme reversible thermodynamic phenomena
Rapposelli and Agostino [49]	(a) Employed thermodynamic relations to extract speed of sound for various liquids
	(b) Captures most features of bubble dynamics well
Utturkar *et al.* [25]	(a) Solved energy equation in the entire domain with dynamic update of material properties
	(b) Test results for different fluids and reference conditions were consistent with the experimental results

DOI: 10.1002/fld

predictions. These material properties are typically obtained from the models developed using the experimental data and, naturally, contain uncertainties. The numerical approach employed in the present study has been previously tested and documented against different flow problems [25, 28, 29]. Our focus here is to address the validation aspect, namely, to what extent a transport-based cavitation model can reproduce the cryogenic cavitation physics and how can we improve its performance. Furthermore, realizing that the fluid properties and thermal environments add further challenges to cavitation models, the interplay between fluid and flow characteristics will also be probed.

1.4. Surrogate modeling framework

To facilitate the formulation of a suitable mathematical framework to probe the global sensitivity [50] of the above-mentioned cavitation model and uncertainties in fluid properties in cryogenic environment, we first construct suitable surrogate models [7]. Since the fidelity of surrogate models is critical in determining the success of sensitivity analysis and model validation, we adopt multiple surrogate models to help ascertain the performance measures. There are alternative surrogate models (for example, polynomial response surface (PRS), kriging (KRG), etc.) but the model that best represents a particular function is not known *a priori*. Consequently, the predictions using different surrogate models have a certain amount of uncertainty. Goel *et al.* [51] suggested that the simultaneous use of multiple surrogate models may be beneficial to quantify and to reduce uncertainties in predictions. They also proposed a cross-validation-error-based weighted average surrogate model that was shown to represent a wide variety of test problems very well. The global cross-validation error used in [51] is also known as predicted residual sum of squares (PRESS) in PRS approximation terminology. In this study, we used four surrogate models, PRS approximation, KRG, radial basis neural network (RBNN), and PRESS-based weighted average surrogate (PWS) model constructed using these three surrogates.

These surrogate models are used to calibrate the model parameters of the present transport-based cavitation model [14] in cryogenic conditions. Although the surrogate model approach has become popular for fluid device optimization [7, 8, 52], its application in CFD model validation and improvement has not yet been actively pursued. The present work represents such an endeavor.

1.5. Scope and organization

Specifically, the objectives of this paper are:

(i) To study the physical aspects of cavitation dynamics in cryogenic environment and perform model (and code) validation,
(ii) to conduct a global sensitivity analysis (GSA) to assess the sensitivity of the response to temperature-dependent material properties and model parameters, and
(iii) to calibrate the parameters of a transport-based cryogenic cavitation model for suitable flow conditions and to account for different fluid properties.

The organization of this paper is as follows. The governing equations and the numerical approach followed in this paper are described in Section 2. We present results of GSA to measure the relative importance of different model parameters and uncertainties in material properties and calibration of model parameters in Section 3. The influence of thermal effects on the cavitation model is studied in detail in Section 4. We recapitulate the major findings of the paper in Section 5.

DOI: 10.1002/fld

2. GOVERNING EQUATIONS AND NUMERICAL APPROACH

The set of governing equations for cryogenic cavitation under the homogeneous-fluid modeling strategy comprises the conservative form of the Favre-averaged Navier–Stokes equations, the enthalpy equation, the k–ε two-equation turbulence closure, and a transport equation for the liquid volume fraction. The mass-continuity, momentum, enthalpy, and cavitation model equations are given as follows:

$$\frac{\partial \rho_{\mathrm{m}}}{\partial t}+\frac{\partial(\rho_{\mathrm{m}} u_j)}{\partial x_j}=0 \tag{3}$$

$$\frac{\partial(\rho_{\mathrm{m}} u_i)}{\partial t}+\frac{\partial(\rho_{\mathrm{m}} u_i u_j)}{\partial x_j}=-\frac{\partial p}{\partial x_i}+\frac{\partial}{\partial x_j}\left[(\mu+\mu_{\mathrm{t}})\left(\frac{\partial u_i}{\partial x_j}+\frac{\partial u_j}{\partial x_i}-\frac{2}{3}\frac{\partial u_k}{\partial x_k}\delta_{ij}\right)\right] \tag{4}$$

$$\frac{\partial}{\partial t}[\rho_{\mathrm{m}}(h+f_{\mathrm{v}}L)]+\frac{\partial}{\partial x_j}[\rho_{\mathrm{m}} u_j(h+f_{\mathrm{v}}L)]=\frac{\partial}{\partial x_j}\left[\left(\frac{\mu_{\mathrm{m}}}{Pr_{\mathrm{m}}}+\frac{\mu_{\mathrm{t}}}{Pr_{\mathrm{t}}}\right)\frac{\partial h}{\partial x_j}\right] \tag{5}$$

$$\frac{\partial \alpha_{\mathrm{l}}}{\partial t}+\frac{\partial(\alpha_{\mathrm{l}} u_j)}{\partial x_j}=\dot{m}^{+}+\dot{m}^{-} \tag{6}$$

where ρ_{m} is the density of the fluid–vapor mixture, u_j denotes the components of velocity, p is the pressure, μ_{m} and μ_{t} are the mixture laminar and turbulent viscosities, respectively, h is the sensible enthalpy, f_{v} is the vapor mass fraction, L is the latent heat of vaporization, Pr is the Prandtl number, α_{l} is the fraction of liquid in the mixture, and $\dot{m}^{+}$ and $\dot{m}^{-}$ are the source terms for the cavitation model. The subscript 't' denotes turbulent properties, 'l' represents the liquid state, 'v' represents the vapor state, and 'm' denotes the mixture properties. The mixture property ϕ_{m}, sensible enthalpy, and the vapor mass fraction are, respectively, expressed as

$$\phi_{\mathrm{m}}=\phi_{\mathrm{l}}\alpha_{\mathrm{l}}+\phi_{\mathrm{v}}(1-\alpha_{\mathrm{l}}) \tag{7}$$

$$h=C_{P\mathrm{m}}T \tag{8}$$

$$f_{\mathrm{v}}=\frac{\rho_{\mathrm{v}}(1-\alpha_{\mathrm{l}})}{\rho_{\mathrm{m}}} \tag{9}$$

For the problems studied here, we neglect the effects of kinetic energy and viscous dissipation terms in the energy equation (5) ($O(Re^{-0.5})$, $Re\sim O(10^6)$) because the temperature field in cryogenic cavitation is mainly dictated by the phenomenon of evaporative cooling (refer to Section 4.2).

2.1. Transport-based cavitation model

Physically, the cavitation process is governed by thermodynamics and kinetics of the phase change process. The liquid–vapor conversion associated with the cavitation process is modeled through $\dot{m}^{+}$ and $\dot{m}^{-}$ terms in Equation (6), which represent condensation and evaporation, respectively. The particular form of these phase transformation rates, which in the case of cryogenic fluids also dictate the heat transfer process, forms the basis of the cavitation model. The liquid–vapor condensation rates for the present transport-based cavitation model [14] are

$$\dot{m}^{-}=\frac{C_{\mathrm{dest}}\rho_{\mathrm{l}}\mathrm{Min}(0,\, p-p_{\mathrm{v}})\alpha_{\mathrm{l}}}{\rho_{\mathrm{v}}(0.5\rho_{\mathrm{l}}U_{\infty}^2)t_{\infty}},\quad \dot{m}^{+}=\frac{C_{\mathrm{prod}}\,\mathrm{Max}(0,\, p-p_{\mathrm{v}})(1-\alpha_{\mathrm{l}})}{(0.5\rho_{\mathrm{l}}U_{\infty}^2)t_{\infty}} \tag{10}$$

DOI: 10.1002/fld

where C_{dest} and C_{prod} are the empirical model parameters controlling the evaporation and condensation rates, p_{v} is the vapor pressure, ρ_{v} and ρ_{l} are the vapor and liquid densities, U_∞ is the reference velocity scale, and t_∞ is the reference time scale, defined as the ratio of the characteristic length scale D to the reference velocity scale U_∞ ($t_\infty = D/U_\infty$). Merkle *et al.* [14] validated this cavitation model with the experimental data for non-cryogenic fluids (e.g. water) and specified $C_{\text{dest}} = 1.0$ and $C_{\text{prod}} = 80.0$ as optimal model parameters (referred here as 'original' parameters). However, Utturkar [29] and Hosangadi and Ahuja [30] found that the previously calibrated values of the Merkle *et al.* [14] cavitation model ($C_{\text{dest}} = 1.0$ and $C_{\text{prod}} = 80.0$) are inadequate to provide a good match with the experimental data under the cryogenic condition. Consequently, Utturkar *et al.* [25] suggested $C_{\text{dest}} = 0.68$ and $C_{\text{prod}} = 54.4$ via numerical experimentation, as more appropriate model parameters for liquid nitrogen. However, they noted difficulties in the simultaneous prediction of the temperature and pressure profiles on the surface of the test geometry. The present efforts represent advances in the practice of multi-surrogate model approach for code validation.

2.2. *Thermodynamic effects*

The evaporation and condensation processes result in absorption and release of the latent heat of vaporization that regulates the thermal effects. Furthermore, there is a significant variation in the physical properties ($\rho_{\text{l}}, \rho_{\text{v}}, p_{\text{v}}, \mu, C_P, K,$ and L) with temperature [31] in the operating range that manifests coupling between different governing equations and underscores the importance of thermal effects in cryogenic cavitation. As indicated by phase diagram in Figure 1(d), the physical properties (liquid and vapor densities) are much stronger functions of temperature than pressure, and one can fairly assume the respective phase values on the liquid–vapor saturation curve at a given temperature.

We illustrate the impact of thermal effects in cryogenic environment due to phase change on temperature predictions, and thermo-sensible material properties on temperature and pressure predictions by analyzing energy equation and cavitation sources terms. Firstly, we separate the latent heat terms in the energy equation (Equation (5)) onto the right-hand side to obtain temperature-based form of the energy equation as follows:

$$\frac{\partial}{\partial t}[\rho_{\text{m}} C_{P\text{m}} T] + \frac{\partial}{\partial x_j}[\rho_{\text{m}} u_j C_{P\text{m}} T] = \frac{\partial}{\partial x_j}\left[C_{P\text{m}}\left(\frac{\mu_{\text{m}}}{Pr_{L\text{m}}} + \frac{\mu_{\text{t}}}{Pr_{\text{t}}}\right)\frac{\partial T}{\partial x_j}\right] - \underbrace{\left\{\frac{\partial}{\partial t}[\rho_{\text{m}}(f_{\text{v}} L)] + \frac{\partial}{\partial x_j}[\rho_{\text{m}} u_j (f_{\text{v}} L)]\right\}}_{\text{energy source/sink term}} \tag{11}$$

As can be seen from Equation (11), the 'lumped' latent heat terms manifest as a non-linear source term into the energy equation and physically represent the latent heat transfer rate or the influence of phase change during evaporation and condensation. The spatial variation of thermodynamic properties and the evaporative cooling effect are intrinsically embedded into this transport-based source term causing a coupling of all the governing equations.

The influence of thermal effects due to thermo-sensible material properties can be further analyzed by studying the cavitation source terms (Equation (10)) more closely. Firstly, we consider

DOI: 10.1002/fld

a case when $p-p_v<0$, i.e. $\dot{m}^+=0$, and the evaporation source term can be expressed as

$$\dot{m}^- = \frac{C_{dest}\alpha_l}{t_\infty}\left(\frac{\rho_l}{\rho_v}\right)\left(\frac{p-p_v}{0.5\rho_l U_\infty^2}\right)=\beta R(T)\sigma(T) \tag{12}$$

where $\beta=C_{dest}\alpha_l/t_\infty$, R is the temperature-dependent liquid–vapor density ratio, and σ is the cavitation number. Expanding Equation (12) using Taylor's series and utilizing Equation (2), we obtain

$$\dot{m}^- = \beta\left(R(T_\infty)+\left.\frac{dR}{dT}\right|_{T_\infty}\Delta T+\cdots\right)\left(\sigma(T_\infty)+\left.\frac{dp_v}{dT}\right|_{T_\infty}\frac{\Delta T}{0.5\rho_l U_\infty^2}+\cdots\right) \tag{13}$$

$$\dot{m}^- = \beta\left(R(T_\infty)\sigma(T_\infty)+\sigma(T_\infty)\left.\frac{dR}{dT}\right|_{T_\infty}\Delta T+R(T_\infty)\left.\frac{dp_v}{dT}\right|_{T_\infty}\frac{\Delta T}{0.5\rho_l U_\infty^2}+O(\Delta T^2)\right) \tag{14}$$

Similarly, we can perform an analysis of condensation source term for the condition $p-p_v>0$, such that $\dot{m}^-=0$. Then,

$$\dot{m}^+ = \frac{C_{prod}(1-\alpha_l)}{t_\infty}\left(\frac{p-p_v}{0.5\rho_l U_\infty^2}\right)=\gamma\sigma(T) \tag{15}$$

where $\gamma=C_{prod}(1-\alpha_l)/t_\infty$. As before, using Taylor's series,

$$\dot{m}^+ = \gamma\left(\sigma(T_\infty)+\left.\frac{dp_v}{dT}\right|_{T_\infty}\frac{\Delta T}{0.5\rho_l U_\infty^2}+O(\Delta T^2)\right) \tag{16}$$

It can be concluded from Equations (14) and (16) that the thermal effects influence the cavitation source terms in two ways: (i) thermal rate of change of liquid–vapor density ratio $dR/dT|_{T_\infty}$, which is negative (Figure 1(b)), and (ii) thermal rate of change of vapor pressure $dp_v/dT|_{T_\infty}$ which is positive (Figure 1(a)), thus illustrating competing influences of thermal effects. It is obvious that the degree of influence of thermal effects depends on the choice of operating fluid and the operating conditions (T_∞, p_∞) due to the non-linear variation of material properties with temperature.

2.3. Speed of sound (SoS) model

Numerical modeling of sound propagation is a very important factor in accurate prediction of cavitation in liquid–vapor multiphase mixture. The speed of sound affects the numerical calculation via the pressure correction equation by conditionally endowing it with a convective–diffusive form in the mixture region. Past studies [20, 21, 53] discuss in detail the modeling options, their impact, and issues. The SoS model used here is outlined below,

$$\text{SoS}=C_\rho=C(1-\alpha_l) \tag{17}$$

The density correction term in the continuity equation is thus coupled to the pressure correction term as shown below

$$\rho'=C_\rho p' \tag{18}$$

DOI: 10.1002/fld

In the pure liquid region, we recover the diffusive form of the pressure equation. Senocak and Shyy [19, 20] suggested an $O(1)$ value for the constant C to expedite the convergence of the iterative computational algorithm. However, their recommendation is valid under normalized values for inlet velocity and liquid density. Since we employ dimensional form of equations for cryogenic fluids, we suggest an $O(1/U_\infty^2)$ value for C [29], which is consistent with the above suggestion in terms of the Mach number regime.

2.4. Turbulence model

The k–ε two-equation turbulence model with wall functions is presented as follows [54]:

$$\frac{\partial(\rho_m k)}{\partial t}+\frac{\partial(\rho_m u_j k)}{\partial x_j}=P_t-\rho_m\varepsilon+\frac{\partial}{\partial x_j}\left[\left(\mu+\frac{\mu_t}{\sigma_k}\right)\frac{\partial k}{\partial x_j}\right] \tag{19}$$

$$\frac{\partial(\rho_m \varepsilon)}{\partial t}+\frac{\partial(\rho_m u_j \varepsilon)}{\partial x_j}=C_{\varepsilon_1}\frac{\varepsilon}{k}P_t-C_{\varepsilon_2}\rho_m\frac{\varepsilon^2}{k}+\frac{\partial}{\partial x_j}\left[\left(\mu+\frac{\mu_t}{\sigma_\varepsilon}\right)\frac{\partial \varepsilon}{\partial x_j}\right] \tag{20}$$

The turbulence production term (P_t) and the Reynolds stress tensor are defined as

$$\begin{aligned} P_t &= \tau_{ij}\frac{\partial u_i}{\partial x_j}, \quad \tau_{ij}=-\overline{\rho_m u_i' u_j'} \\ \rho_m u_i' u_j' &= \frac{2\rho_m k\delta_{ij}}{3}-\mu_t\left(\frac{\partial u_i}{\partial x_j}+\frac{\partial u_j}{\partial x_i}\right) \end{aligned} \tag{21}$$

The parameters for this model, $C_{\varepsilon_1}=1.44$, $C_{\varepsilon_2}=1.92$, $\sigma_\varepsilon=1.3$, and $\sigma_k=1.0$, are adopted from the equilibrium shear flow calibration [55], and the turbulent viscosity is defined as

$$\mu_t=\frac{\rho_m C_\mu k^2}{\varepsilon}, \quad C_\mu=0.09 \tag{22}$$

Of course, the turbulence closure and the eddy viscosity levels can affect the outcome of the simulated cavitation dynamics, especially in the case of unsteady simulations. For detailed investigations of turbulence modeling on cavitating flow computations, we refer to recent works by Wu *et al.* [56] and Utturkar *et al.* [28]. Vaidyanathan *et al.* [57] conducted a sensitivity analysis to assess the interplay between turbulence model parameters and cavitation model parameters in non-cryogenic environment. They observed that multiple combinations of turbulence parameters and cavitation model parameters yield the same performance.

To appraise the influence of turbulence modeling on the current problem, we follow the previous investigation by Vaidyanathan *et al.* [57] and compare the standard k–ε turbulence model and a non-equilibrium k–ε turbulence model developed by Shyy *et al.* [55] that accounts for the absence of equilibrium between the production and destruction of dissipation of turbulent kinetic energy. Both turbulence models offered very similar predictions within the experimental uncertainties (Appendix A). Hence, we restrict the scope of this study to the calibration of cryogenic cavitation model parameters with the standard k–ε turbulence model.

2.5. Numerical approach

The governing equations are numerically solved using a CFD code STREAM [58] based on a pressure-based algorithm and the finite-volume approach [19, 55, 58, 59]. We use multi-block,

DOI: 10.1002/fld

structured, curvilinear grids to analyze flow over different geometries in this paper. The viscous terms are discretized by second-order accurate central differencing, whereas the convective terms are approximated by the second-order accurate controlled variations scheme (CVS) [60]. The use of CVS scheme can enhance the second-order upwind scheme [61] and prevents oscillations under sharp gradients caused by the evaporation source term in the cavitation model, while retaining second order of formal accuracy. The pressure–velocity coupling is implemented through the extension of the SIMPLEC [62] type of algorithm cast in a combined Cartesian-contravariant formulation [58] for the dependent and flux variables, respectively, followed by adequate relaxation for each governing equation, to obtain steady-state results. The temperature-dependent material properties are updated from the NIST [31] database at the end of each computational iteration.

3. RESULTS AND DISCUSSION

3.1. Test geometry, boundary conditions, and performance indicators

We simulate flows over a 2D hydrofoil and an ogive in cryogenic environment, which serve as the benchmark problems for validating the cryogenic cavitation models. Hord [35, 39] experimentally investigated the flow over these geometries inside suitably designed wind tunnels (Figure 2(a)). He reported average pressure and temperature data at five probe locations over the body surface for different cases that are referenced alpha-numerically [35, 39]. We employ (i) Case '290C' for liquid nitrogen ($Re = 9.1 \times 10^6$, $\sigma_\infty = 1.7$, $T_\infty = 83.06\,\mathrm{K}$, liquid–vapor density ratio=95, hydrofoil) and (ii) Case '249D' for liquid hydrogen ($Re = 2.0 \times 10^7$, $\sigma_\infty = 1.57$, $T_\infty = 20.70\,\mathrm{K}$, liquid–vapor density ratio = 47, hydrofoil) to conduct optimization and sensitivity studies.

A simplified geometry, schematic computational domain, and the boundary conditions for the two test problems are shown in Figure 2. The computational grid consists of 320×70 and 340×70 non-uniformly distributed grid points for the hydrofoil and the ogive, respectively, such that the cavitation regime is adequately resolved and the deployment of wall functions near the no-slip boundary conditions is allowed [25]. The inlet boundary conditions are implemented by stipulating the values of the velocity components, phase fraction, temperature, and turbulence quantities from the experimental data [35]. At the walls, pressure, phase fraction, and turbulence quantities are extrapolated, along with applying the no-slip (in the form of the wall function [62]) and adiabatic conditions on the velocity and temperature, respectively. Pressure and other variables are extrapolated at the outlet boundaries while enforcing global mass conservation by rectifying the outlet velocity components. In addition, we hold the pressure at the reference point (illustrated in the experimental reports [35, 39]) constant at the reference value specified by the experiments. Although the cavitating flows are unsteady in nature, no time-dependent data were reported by Hord. Utturkar [29] showed that the flows considered here can be modeled as steady state. Furthermore, for sheet cavitating flows, it has been shown by Senocak and Shyy [19] that steady-state computations can well capture the essential flow features and reach close agreement with the measurements. Consequently, we modeled the flow as steady state.

The quality of the predictions is numerically quantified by computing the L_2 norms of the differences between computed and experimental values of pressure (P_{diff}) and temperature (T_{diff}) at each of the five probe locations on the surface of hydrofoils. These metrics are desired to be low to obtain good prediction quality.

DOI: 10.1002/fld

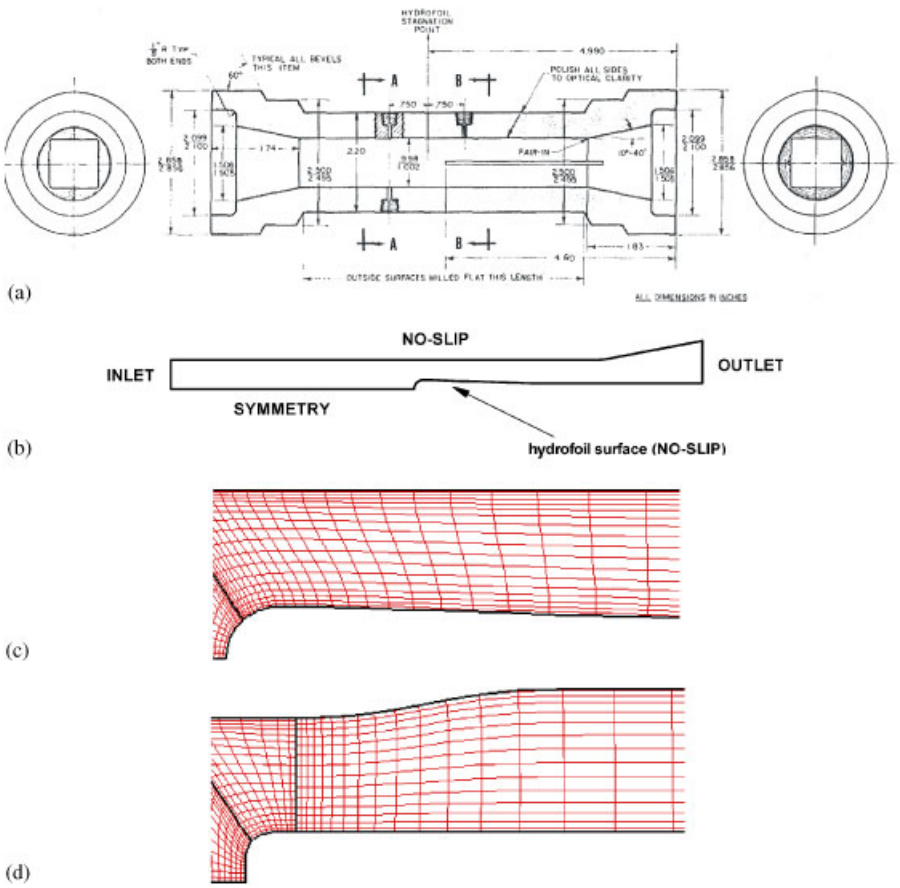

Figure 2. Experimental setup and computational geometries: (a) experimental setup used by Hord [35, 39] to conduct cryogenic cavitation experiments over hydrofoil and ogive geometries; (b) a schematic of the computational setup; (c) the geometry of the adopted hydrofoil; and (d) the geometry of the adopted 0.357-in ogive.

3.2. Surrogate-based global sensitivity assessment and calibration

Since minor changes in flow environment can lead to substantial changes in the predictions in cryogenic environment [25], it is imperative to appraise the role of model parameters and uncertainties in material properties on the predictions. In this section, we characterize the parameters that significantly affect predictions using surrogate-based GSA and then calibrate the cryogenic cavitation model parameters. In the following, we present in detail the process of model parameter optimization and sensitivity evaluations based on Case '290C' for liquid nitrogen. A corresponding study based on Case '249D' for hydrogen has also been carried out. To save space, we do not repeat the detailed information and report only the outcome.

3.2.1. Global sensitivity assessment. We employ variance-based, non-parametric GSA method, proposed by Sobol [50] (refer to Appendix B), to evaluate the sensitivity of cryogenic cavitation

DOI: 10.1002/fld

model with respect to model parameters and material properties and to obtain an insight about the factors that influence the accuracy of predictions. We can study the influence of uncertainty in different material properties, ρ_v, ρ_l, K, C_p, and L, and model parameters C_{dest}, C_{prod}, and t_∞. However, to keep Re (Reynolds number based on upstream flow) and σ_∞ (cavitation number based on upstream flow) constant for the given case and to keep the computational expense reasonable, we select one material property from energy equation and cavitation transport α-equation. Consequently, we choose $C_{dest}, C_{prod}, \rho_v$, and L as variables. The model parameters, C_{dest} and C_{prod}, are perturbed on either side of the values proposed by Utturkar *et al.* [25] ($C_{dest}=0.68, C_{prod}=54.4$) by 15% and the material properties, ρ_v and L, are perturbed within 10% of the values they assume from the NIST database [31] (perturbations are denoted as ρ_v^* and L^*). The ranges of the variables are given in Table II. The performance of the cryogenic cavitation model is characterized by prediction errors P_{diff} and T_{diff}, defined in Section 3.1.

To conduct GSA, the response function is decomposed into additive functions of variables and interactions among variables. This allows the total variance (V) in the response function to be expressed as a combination of the main effect of each variable (V_i) and its interactions with other variables (V_{iZ}). The sensitivity of the response function with respect to any variable is measured by computing its sensitivity indices. The sensitivity indices of main effect (S_i) and total effect (S_i^{total}) of a variable are given as follows:

$$S_i = V_i / V, \quad S_i^{total} = (V_i + V_{iZ}) / V \tag{23}$$

3.2.1.1. Surrogate construction. In the absence of a closed-form solution characterizing the objective functions (P_{diff} and T_{diff}), different components of variances are evaluated using numerical integration. Since direct coupling of CFD simulations with numerical integration schemes is computationally expensive, we use surrogate models of the performance indicators. We evaluate the responses P_{diff} and T_{diff} using CFD simulations at 70 data points (combinations of variables) selected via face-centered cubic composite design (FCCD, 25 points) and Latin hypercube sampling (LHS, 45 points) experimental designs. We construct four surrogates: PRS approximation, KRG, RBNN, and a PWS model (refer to Appendix C) of both responses in scaled variable space (all variables are scaled between zero and one, such that zero corresponds to the minimum value). We use reduced cubic polynomials for PRS and a spread coefficient = 0.5 for RBNN. Relevant details of the quality of fit of surrogate models are summarized in Table III. Low PRESS and low root mean square error compared with the range of the function indicate that the two responses are adequately approximated by the surrogate models. For both objectives, RBNN surrogate is

Table II. Ranges of variables for global sensitivity analyses.

Variable	Minimum	Baseline	Maximum
C_{dest}	0.578	0.68	0.782
C_{prod}	46.24	54.4	62.56
ρ_v^*	0.90	1.0	1.10
L^*	0.90	1.0	1.10

C_{dest} and C_{prod} are the model parameters associated with the cavitation model source terms for liquid nitrogen, and ρ_v and L^* are the multiplication factors of vapor density and latent heat obtained from NIST database [31], respectively.

DOI: 10.1002/fld

Table III. Summary of surrogate approximations of prediction metrics P_{diff} and T_{diff}.

Surrogate	Parameter	P_{diff}	T_{diff}
	Number of training points	70	70
	Minimum of data	1.653	0.334
	Mean of data	3.984	0.462
	Maximum of data	9.000	0.673
PRS	Number of coefficients	23	19
	R^2_{adj}	0.979	0.954
	PRESS	0.344	0.0136
	Maximum error	0.609	0.0285
	RMS error	0.297	0.0121
KRG	Process variance	1.277	1.67e−3
	PRESS	0.166	6.92e−3
RBNN	PRESS	1.538	0.0726
	Maximum error	0.0905	8.64e−3
PWS	PRESS	0.227	9.56e−3
	Maximum error	0.199	9.64e−3

Note: PRS, polynomial response surface; KRG, Kriging; RBNN, radial basis neural network; PWS, PRESS-based weighted surrogate (PRESS is the square root of predicted residual sum of squares). The test example is Case 290C (liquid nitrogen flow over hydrofoil).

Table IV. Weights associated with different surrogate models (four design variables, 70 data points).

Objective	w_{prs}	w_{krg}	w_{rbnn}
P_{diff}	0.320	0.603	0.077
T_{diff}	0.335	0.597	0.068

the worst of the three surrogates and KRG is the best (compare PRESS errors). The contribution of different surrogate models to the PWS model, given by the weights in Table IV, accounts for the poor performance of RBNN by assigning it a low weight. We employ the Gauss-quadrature integration scheme, with 10 Gaussian points along each direction, to evaluate sensitivity indices. Responses at Gaussian points are evaluated using surrogate models.

The influence of the choice of surrogate model on the prediction of sensitivity indices is illustrated in Figure 3 with the help of main effects for P_{diff}. Since all surrogates predict similar trend about the importance of different variables, we may conclude that the variability in predictions due to the choice of surrogate model is small.

3.2.1.2. Main and interaction effects of different variables. We show sensitivity indices of main effects and total effects (estimated via PWS model) in Figure 4 to quantify the relative importance of different parameters on P_{diff} and T_{diff}. The sensitivity indices of the main effects (pie-charts) suggest that C_{dest} is the most influential, and C_{prod} is the least influential parameter within the selected range of variation, i.e. the cavity morphology is more influenced by

DOI: 10.1002/fld

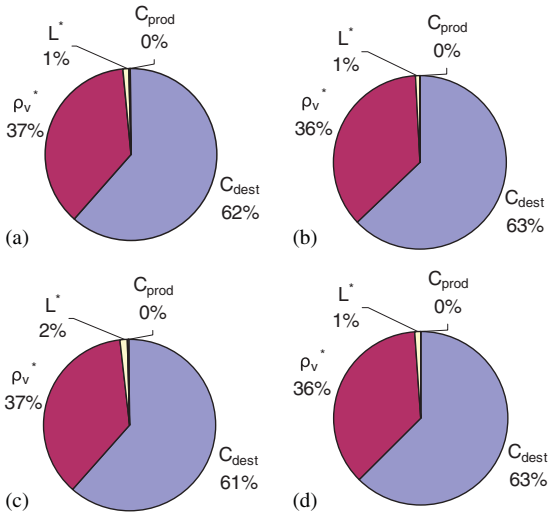

Figure 3. Sensitivity indices of main effects using multiple surrogates of prediction metric P_{diff} (liquid N_2, Case 290C): (a) polynomial response surface; (b) Kriging; (c) radial basis neural networks; and (d) PRESS-based weighted surrogate.

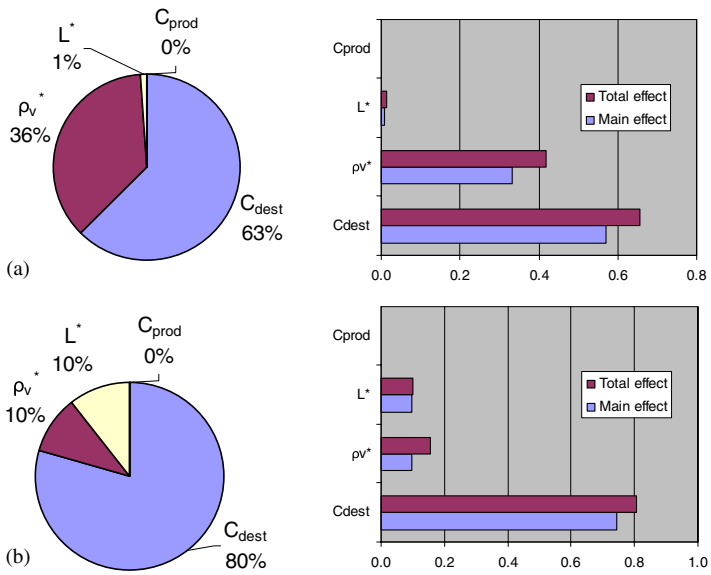

Figure 4. Influence of different variables on performance metrics (a) P_{diff} and (b) T_{diff} quantified using sensitivity indices of main and total effects. We show results obtained using PWS surrogate (liquid N_2, Case 290C).

the evaporation rate term compared with the condensation term that is influential in determining the pressure recovery rate posterior to cavity closure. The variability due to material properties as indicated by the sensitivity indices associated with vapor density ρ_v and latent heat L

DOI: 10.1002/fld

is smaller compared with the model parameters, but is not negligible. The variability in vapor density ρ_v influences both pressure and temperature predictions, but has more significant impact on pressure predictions. On the other hand, the variability in latent heat (L) within the selected uncertainty range affects temperature predictions only. Relatively moderate influence of variation in latent heat on temperature predictions does not lead to significant variation in pressure predictions because the latter is more significantly influenced by the parameters that directly appear in cavitation source terms and have more pronounced effect. The differences between the main and the total sensitivity indices for both P_{diff} and T_{diff} highlight the importance of interaction among parameters. The interaction between C_{dest} and ρ_v is particularly stronger than other parameters.

3.2.1.3. Validation of GSA. We validate the results of GSA by evaluating the variation in responses P_{diff} and T_{diff} when only one parameter is changed at a time and the remaining parameters are fixed at their mean values (mean of the selected range). We assign six equispaced levels for each variable and calculate the variation in responses using Abramowitz and Stegun six-point numerical integration scheme [63] that has seventh-order accuracy. The sensitivity indices of main effects of different parameters on P_{diff} and T_{diff} are shown in Figure 5. The results obtained by actual computations are in sync with the findings of the GSA, that is, the model parameter C_{dest} and the uncertainty in vapor pressure ρ_v are the most influential parameters for accurate pressure and temperature predictions, and the uncertainty in latent heat L is important only for predicting temperature accurately. The differences in the actual magnitude of sensitivity analysis results can be explained by accounting for (i) the small number of points used for actual sensitivity computations, (ii) the neglect of interaction terms, and (iii) the errors in surrogate modeling. Nevertheless, the important trends in the results are captured adequately.

The results indicate that the performance of cryogenic cavitation model is more susceptible to variability in temperature-dependent vapor density ρ_v compared with the variability in latent heat L. This calls for more attention in developing accurate models of ρ_v. Also, the variables that appear in cavitation source terms ($\dot{m}^-$ or $\dot{m}^+$) may tend to register greater influence on the computed results. Thus, intuitively, reference velocity U_∞, reference time scale t_∞, and liquid density ρ_l, which are omitted from the present GSA, are expected to induce large variability in the computation compared with other omitted properties such as thermal conductivity K and specific heat C_p. Furthermore, as depicted by sensitivity indices in Figure 4, largely the impact of different

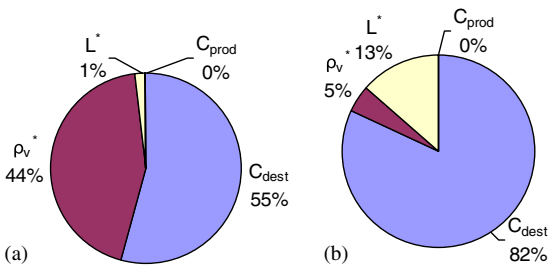

Figure 5. Validation of global sensitivity analysis results for main effects of different variables on P_{diff} and T_{diff} (liquid N_2, Case 290C): (a) pressure predictions P_{diff} and (b) temperature predictions T_{diff}.

DOI: 10.1002/fld

parameters is expected to be the same on pressure and temperature due to the tight coupling between various flow variables.

3.3. Calibration of cryogenic cavitation model

In the previous section, we observed that one of the model parameters C_{dest} significantly influences the performance of the present cryogenic cavitation model. This information can be used to calibrate the present cavitation model parameters associated with different fluids. Firstly, we optimize the model parameter (C_{dest}) of the present cryogenic cavitation model using the benchmark case of liquid nitrogen flow over a hydrofoil '290C', while fixing the model parameter C_{prod} at 54.4 (minimal influence on predictions), and assuming the temperature-dependent material properties obtained from the NIST database [31] to be accurate.

We observed that increasing C_{dest} increases P_{diff} and decreases T_{diff}. As shown in Figure 6, the parameters that yield good pressure predictions (low P_{diff}) produce large errors in temperature predictions (high T_{diff}) and *vice versa* (low T_{diff} but high P_{diff}). Hence, this model calibration/system identification problem is a multi-objective optimization to simultaneously minimize P_{diff} and T_{diff} by varying the model parameter C_{dest}. Since the cavitation dynamics primarily impacts pressure fluctuations, we seek to improve the pressure prediction capabilities of the present cryogenic cavitation model without incurring a significant deterioration of temperature predictions. Consequently, we allow the model parameter C_{dest} to vary between 0.578 and 0.68.

3.3.1. Surrogate modeling of objectives. To represent the responses P_{diff} and T_{diff} using surrogate models, we sample data using CFD simulations at nine locations. The location of points and the corresponding P_{diff} and T_{diff} shown in Figure 7 clearly exhibit the conflicting nature of the two objectives. As before, we construct PRS, KRG, RBNN, and PWS models. We approximate P_{diff} with a reduced cubic PRS and T_{diff} with a reduced quintic PRS. The relevant metrics, depicting the quality of surrogate models, are summarized in Table V and the weights associated with different surrogates in PWS model are given in Table VI. Low PRESS and low RMS errors indicate that

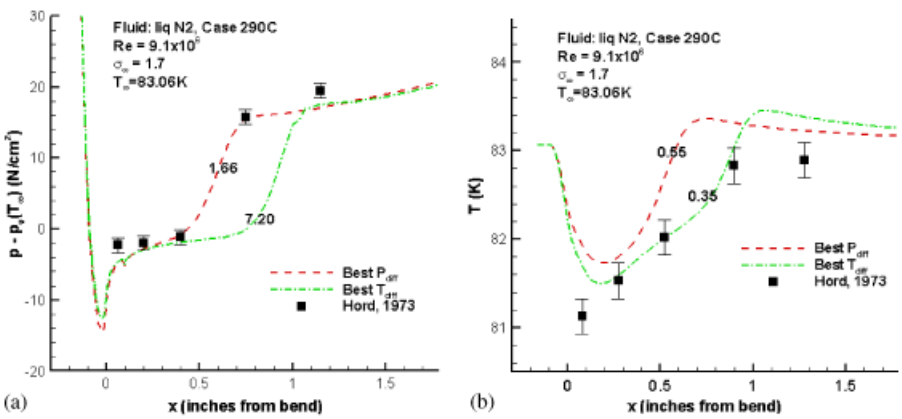

Figure 6. Surface (a) pressure and (b) temperature predictions using the model parameters for liquid N_2 that minimized P_{diff} and T_{diff}, respectively (Case 290C). The number on each surface pressure or temperature profile represents P_{diff} or T_{diff} value associated with appropriate model parameters.

DOI: 10.1002/fld

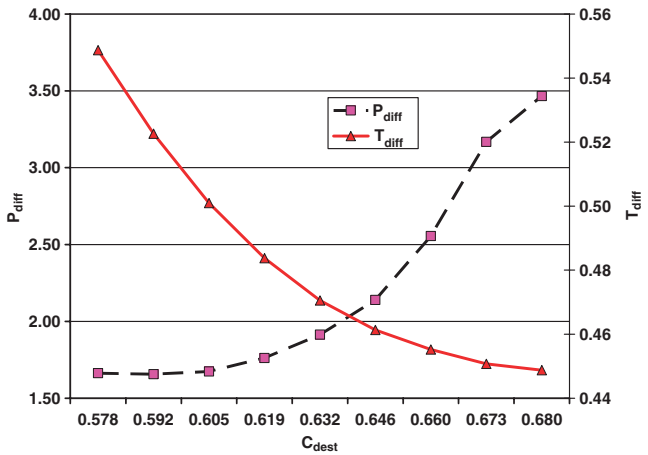

Figure 7. Location of points (C_{dest}) and corresponding responses (P_{diff} is shown on left y-axis, and T_{diff} is shown on right y-axis) used for calibration of the cryogenic cavitation model (liquid N_2, Case 290C).

Table V. Different accuracy measures for surrogate models of P_{diff} and T_{diff}.

Surrogate	Parameter	P_{diff}	T_{diff}
	Number of training points	9	9
	Minimum of data	1.657	0.449
	Mean of data	2.222	0.483
	Maximum of data	3.465	0.549
PRS	Number of coefficients	3	5
	R^2_{adj}	0.999	1.000
	PRESS	0.032	1.05e−4
	Maximum error	0.037	7.00e−5
	RMS error	0.021	6.00e−5
KRG	Process variance	0.098	1.02e−3
	PRESS	0.010	3.98e−4
RBNN	PRESS	0.077	9.00e−3
	Maximum error	0.018	6.28e−3
PWS	PRESS	0.025	3.25e−4
	Maximum error	0.011	1.49e−4

Note: We use a single variable for calibration. PRS, polynomial response surface; KRG, Kriging; RBNN, radial basis neural network; PWS, PRESS-based weighted surrogate (PRESS is the square root of predicted residual sum of squares). The test example is Case 290C (liquid nitrogen flow over hydrofoil).

the two responses are well represented by all surrogate models. Although no single surrogate model performs the best for both responses, RBNN is the worst of the three surrogates considered here. The weights associated with different surrogates in the PWS model also reflect the same. PRESS and maximum error measures indicate that the PWS model obtained by averaging different

DOI: 10.1002/fld

Table VI. Weights associated with different surrogate models (single variable, 9 points).

	w_{prs}	w_{krg}	w_{rbnn}
P_{diff}	0.239	0.659	0.101
T_{diff}	0.666	0.315	0.019

Note: PRS, polynomial response surface approximation; KRG, Kriging; RBNN, radial basis neural network.

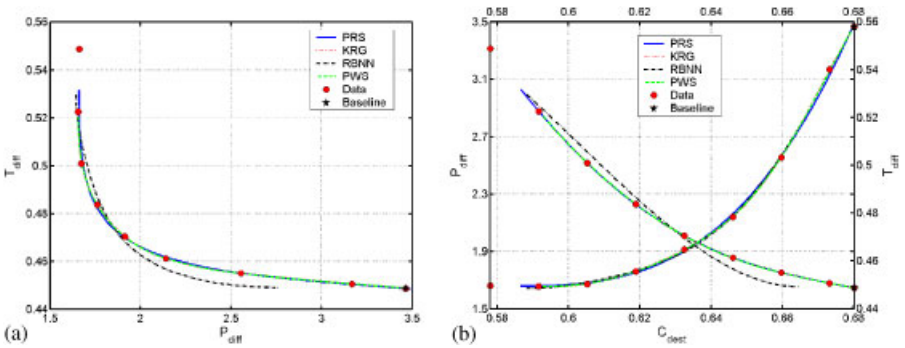

Figure 8. Pareto optimal front (POF) and corresponding optimal points in (a) function space and (b) variable space (liquid N_2, Case 290C). PRS, polynomial response surface; KRG, Kriging; RBNN, radial basis neural network; PWS, PRESS-based weighted average surrogate.

surrogate models performs significantly better than the worst surrogate and the performance is comparable to the best surrogate.

3.3.2. Multi-objective optimization. We convert the present multi-objective optimization problem into a single objective optimization problem by combining the two performance metrics (P_{diff} and T_{diff}) using weights (weighted sum strategy [64]) or by treating one performance metric as an objective function and the second performance metric as a constraint function (ε-constraint strategy [65]). We obtain many candidate Pareto optimal solutions by varying the weights for weighted sum strategy and constraint values for ε-constraint strategy. After removing dominated and duplicate solutions from the set of candidate solutions, the function space and the variable space illustration of Pareto optimal front (POF) obtained through different surrogate models is shown in Figure 8. We observe that different POFs obtained by using multiple surrogate models are close to one another in both function and variable spaces. All surrogate models predict that a small increase in T_{diff} will lead to a significant reduction in the P_{diff} (Figure 8(a)). We note that the pressure fluctuations play a more important role in determining the cavity morphology and the loadings on turbomachinery. Consequently, accurate pressure prediction is our primary objective.

We select a trade-off solution on the POF for validation, such that notable reduction in P_{diff} can be realized without incurring significant deterioration of T_{diff}. Corresponding C_{dest} (referred to as the 'best-compromise' parameter) computed (via CFD simulations) and predicted (using surrogate models) responses (P_{diff} and T_{diff}) are given in Table VII. The errors in predictions of P_{diff} and

DOI: 10.1002/fld

Table VII. Predicted and computed P_{diff} and T_{diff} at best-compromise model parameter for liquid N_2 (Case 290C).

C_{dest}		Simulation	PRS	KRG	RBNN	PWS
0.639	P_{diff}	2.012	2.017	2.012	2.003	2.012
	T_{diff}	0.466	0.466	0.465	0.463	0.465

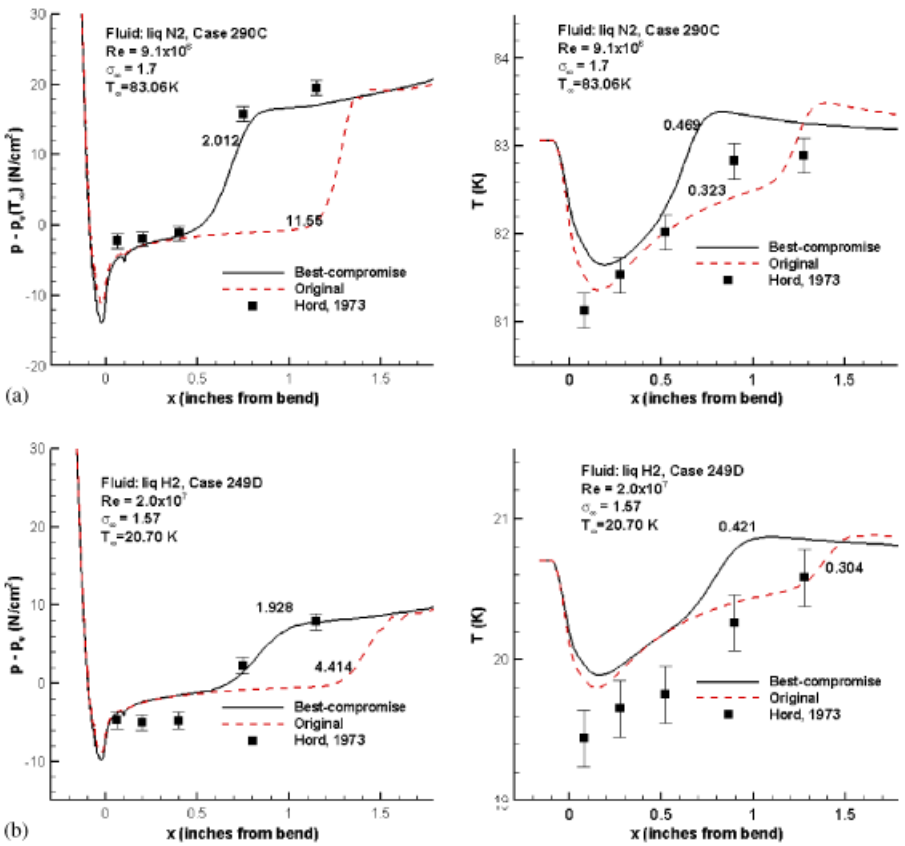

Figure 9. Surface pressure and temperature predictions on benchmark test cases ((a) 290C, hydrofoil, LN2 and (b) 249D, hydrofoil, LH2) using the model parameters corresponding to original and best-compromise values for different fluids. The number on each surface pressure/temperature profile represents P_{diff} or T_{diff} value associated with appropriate model parameters.

T_{diff} are small for all surrogates except RBNN. Clearly, the PWS model yields the best predictions on both objectives. A graphical comparison of surface pressure and temperature profiles obtained with the original [14] and optimal parameters of present transport-based cavitation model is shown in Figure 9(a). The calibrated model parameters yield 72% reduction in P_{diff} by allowing 3.8% increase in T_{diff} compared with the original parameters [14]. The improvements in the surface

DOI: 10.1002/fld

pressure prediction, which is the more important criterion to estimate loadings due to cavitation, are obvious, whereas the deterioration in the temperature predictions is small.

From cavitation dynamics point of view, the main issue with the predictions using original parameters was the poor prediction of the cavity closure region. The best-compromise model parameters reduce the evaporation source term by reducing the model parameter C_{dest}. This change brings favorable changes in the cavity closure region by allowing an earlier onset of condensation and hence faster recovery of the pressure as was observed in experiments.

3.3.3. Optimization outcome for hydrogen. We repeat the model calibration exercise for liquid hydrogen fluid considering case '249D' (hydrofoil) as the benchmark case. The corresponding 'best-compromise' C_{dest} parameter is found to be 0.767. Notably, the ratio of best-compromise and baseline value of C_{dest} for both nitrogen and hydrogen is 0.94. The surface pressure and temperature profiles shown in Figure 9(b) clearly demonstrate the improvements in pressure predictions with the calibrated parameters compared with the original parameters [14].

3.4. Validation of the calibrated cavitation model

The calibrated model parameters of the present cryogenic cavitation model are validated by simulating additional benchmark cases for two geometries (hydrofoil [35] and ogive [39]) using different working fluids, liquid nitrogen and liquid hydrogen. The cases considered in the present paper along with the best-compromise model parameters are enlisted in Table VIII. We compared the surface pressure and temperature profiles predicted using the cryogenic cavitation model with the calibrated (best-compromise) and the original model parameters [14] in Figure 10. The model with best-compromise parameters exhibits substantially more robust performance for different geometries, fluids, and flow environments.

3.5. Comparison of flow fields for original and calibrated model parameters

We compare different flow variables (density, pressure, and temperature) in the field predicted using the original and the calibrated model parameters. We show the results for Case 290C and Case 296B in Figures 11 and 12, respectively. As was observed in the surface pressure and temperature plots, the cryogenic cavitation model using the original model parameters predicted larger cavity for both

Table VIII. Flow cases chosen for the validation of the calibrated cryogenic cavitation model.

Fluid	Geometry	Case name [35, 39]	T_∞ (K)	Re_∞	σ_∞	$\rho_l/\rho_v\|_{T_\infty}$	% Change in $\dot{m}^-$	% Change in $\dot{m}^+$	C_{dest}
Liquid N_2	Hydrofoil	290C	83.06	9.0×10^6	1.70	94.90	−7.58	7.53	0.639
Liquid N_2	Hydrofoil	296B	88.54	1.1×10^7	1.61	56.25	−1.00	12.34	0.639
Liquid N_2	Ogive	312D	83.00	9.0×10^6	0.46	95.47	9.12	19.18	0.639
Liquid H_2	Hydrofoil	249D	20.70	2.0×10^7	1.57	46.97	−14.79	26.57	0.767
Liquid H_2	Hydrofoil	255C	22.20	2.5×10^7	1.49	31.60	−8.96	29.01	0.767
Liquid H_2	Ogive	349B	21.33	2.3×10^7	0.38	39.91	20.96	34.28	0.767

Note: σ_∞ is the cavitation number, Re_∞ is the free-stream Reynolds number, T_∞ is the inlet temperature, ρ_l is the liquid density, ρ_v is the vapor density, $\dot{m}^-, \dot{m}^+$ are evaporation and condensation terms in transport-based cavitation model, and C_{dest} is the best-compromise model parameter.

DOI: 10.1002/fld

cases. The differences in the flow fields clearly indicate that better predictions were obtained using the best-compromise model parameters. We observe that Case 296B (lower free-stream cavitation number) has a bigger cavity with higher liquid content compared with the cavity for Case 290C, which is smaller and contains more vapor. In both cases, we observe a drop in local temperature during evaporation inside the cavity region and a rise in temperature in the condensation (cavity closure) region. The downstream drop in temperature indicates that the heat is carried away via convection. These results are consistent with the analytical assessment shown in Section 2.2.

The results presented here clearly spell the merits of employing a systematic methodology to examine the role of cavitation model parameters. Overall, our results indicate that the type of fluid has more influence on predictions than the geometric and operating parameters. This is because the phase change conditions and thermo-fluid property variations are material dependent, as was shown in Section 2.2. Although we have shown results only for 2D analysis, we expect that the conclusions reached here would be applicable to 3D as well as time-dependent flows.

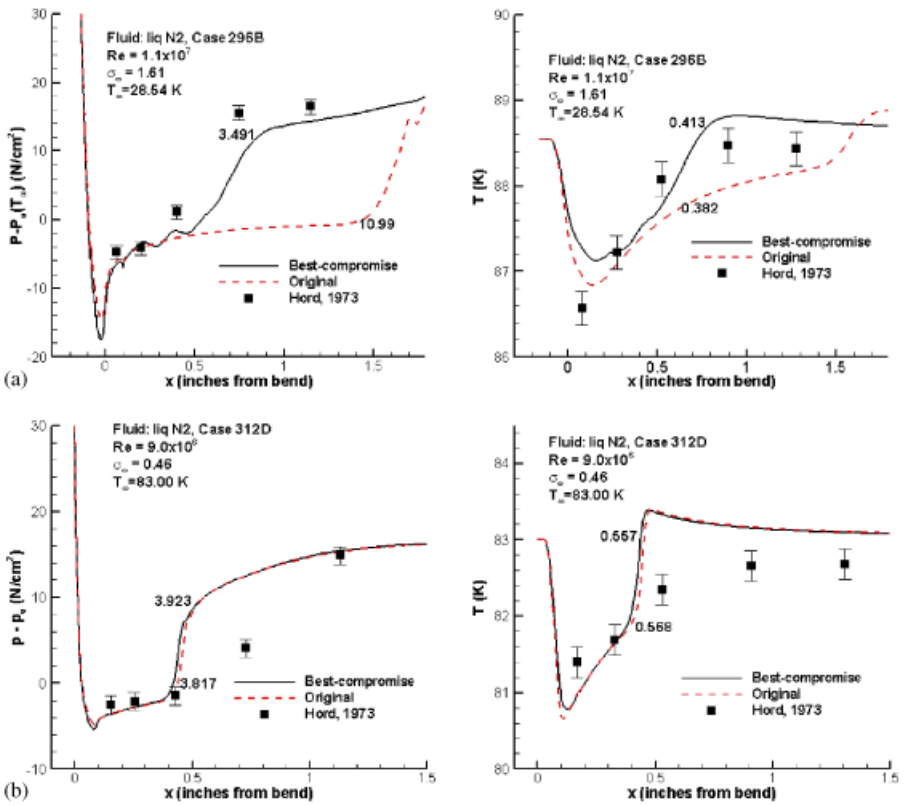

Figure 10. Surface pressure and temperature predictions using the original parameters ($C_{\text{dest}} = 1.0$, $C_{\text{prod}} = 80.0$) and best-compromise parameters ($C_{\text{prod}} = 54.4$, and $C_{\text{dest,LN}_2} = 0.639$ or $C_{\text{dest,LH}_2} = 0.767$). (a) 296B, hydrofoil, LN_2; (b) 312D, ogive, LN_2; (c) 255C, hydrofoil, LH_2; and (d) 349B, ogive, LH_2. The number next to each surface pressure or temperature profile represents P_{diff} or T_{diff} value associated with appropriate model parameters.

DOI: 10.1002/fld

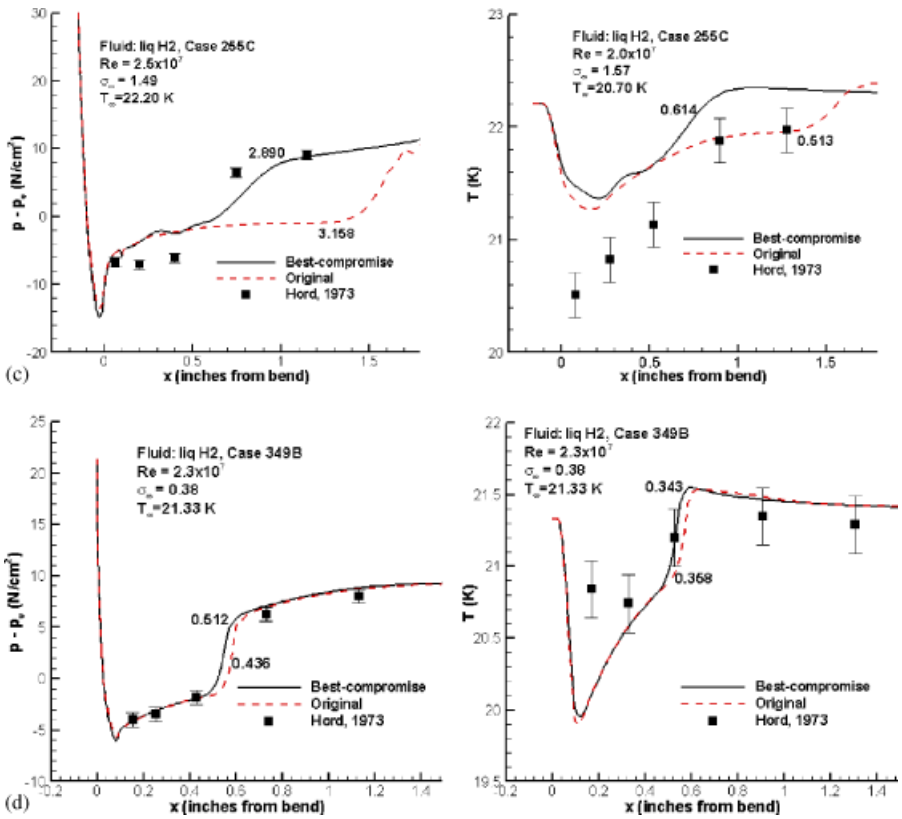

Figure 10. *Continued*.

In the present case, the implications of the optimization on pressure and thermal fields are inconsistent. Although this indicates the merits of adopting a multi-objective optimization framework, as has been conducted here, it also suggests that there is a need for further investigation of the effect of thermal variations on cryogenic cavitating flows and whether the present cavitation and turbulence models capture all essential physical mechanisms or not. It should also be reiterated that in terms of practical impact, the pressure prediction is our primary objective because pressure fluctuation is what causes poor performance or even catastrophic situation in fluid machinery. In the following, we offer further assessment of the thermal effect.

4. INVESTIGATION OF THERMAL EFFECTS AND BOUNDARY CONDITIONS

In the previous section, we observed discrepancies in simultaneous predictions of temperature and pressure. To understand the underlying issues related to thermodynamic effects, we study the influence of thermo-sensitive material properties and the role of thermal boundary condition on the hydrofoil wall for Case 290C. We use the best-compromise values of model parameters (liquid N_2) in all cases. Again, we use standard k–ε turbulence model (refer to Appendix A).

DOI: 10.1002/fld

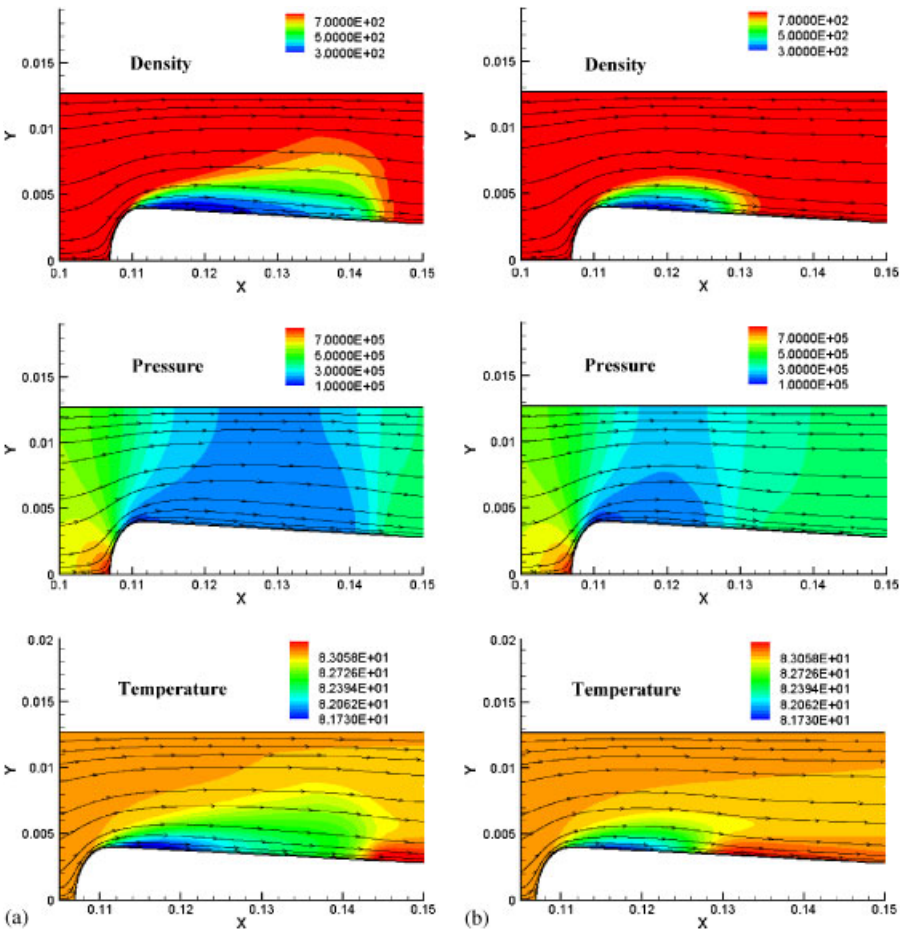

Figure 11. Flow variables for Case 290C for (a) original parameters ($C_{\text{dest}} = 1.0, C_{\text{prod}} = 80.0$) and (b) best-compromise parameters ($C_{\text{dest}} = 0.639, C_{\text{prod}} = 54.4$).

4.1. Influence of thermo-sensitive material properties

Firstly, we highlight the influence of thermal effects via phase change and thermo-sensitive properties on the temperature and pressure predictions in Figure 13. The difference between pressure and free-stream vapor pressure ($p - p_{\text{v}}(T_\infty)$) and the difference between pressure and the actual vapor pressure (based on temperature, $p - p_{\text{v}}(T)$) are shown in Figure 13(a). The cavitation in cryogenic environment differs from non-cryogenic environment in two ways: (i) the under-shoot at the leading edge of the hydrofoil indicates slower pressure recovery in cryogenic environment and the influence of cooling due to heat absorption than that observed in the non-cryogenic environment and (ii) the vapor pressure in the cavity in cryogenic environment is not constant (continuous increase) due to the variation in temperature. This increase in vapor pressure (as marked by Δp_{v} in Figure 13(a)) is attributed to the variation in temperature (Figure 1). The change in vapor pressure affects the cavitation source terms (Equations (14) and (16)) and resultant liquid–vapor

DOI: 10.1002/fld

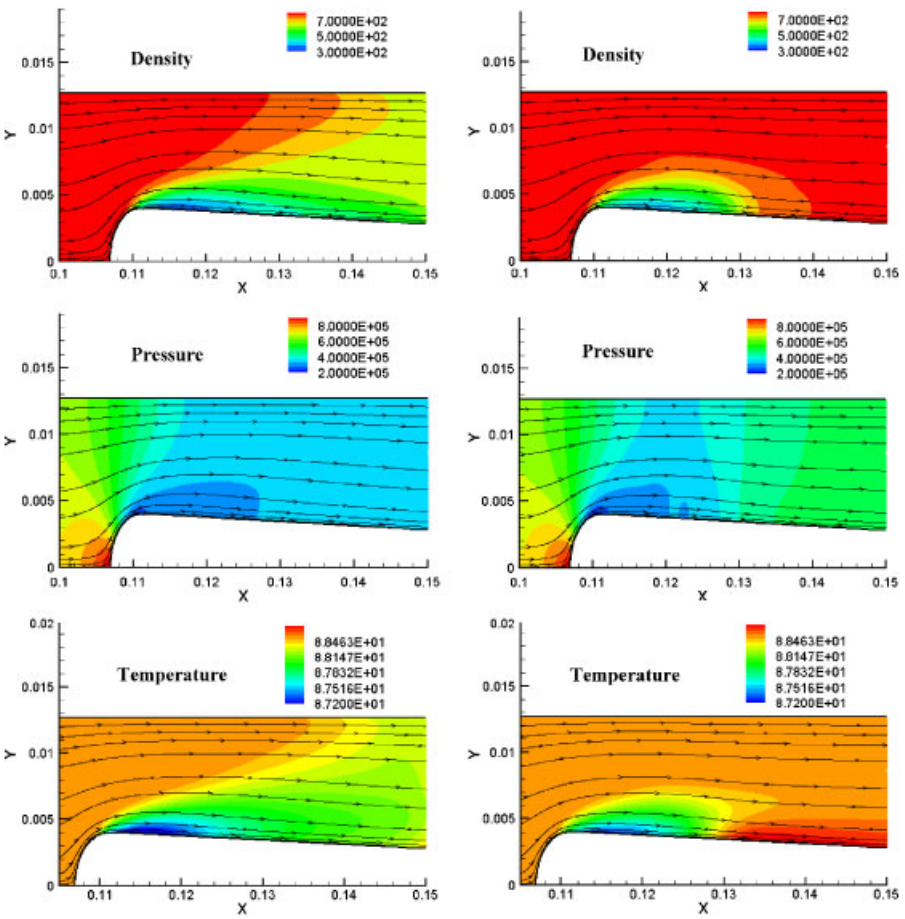

Figure 12. Flow variables for Case 296B for original parameters ($C_{\text{dest}} = 1.0, C_{\text{prod}} = 80.0$) and best-compromise parameters ($C_{\text{dest}} = 0.639, C_{\text{prod}} = 54.4$).

fraction, which impacts the source terms in energy equation to enforce coupling of thermal effects in governing equations. To contrast the thermal effect on the cavitation dynamics, we also show a solution obtained by assigning a zero latent heat in Figure 13(a). With zero latent heat and an adiabatic wall condition, the fluid field exhibits a constant temperature throughout, resulting in a constant vapor pressure. This isothermal cavitation case yields a substantially larger cavity with near constant pressure on the surface inside cavity, which is quite different from the experimental measurement.

The temperature on the surface of hydrofoil in cavitating conditions is shown in Figure 13(b). The significant drop in temperature near the leading edge of the cavity is explained as follows. The phase change, as modeled, is dictated by the vapor pressure. When the local pressure in the flow falls below the vapor pressure, evaporation begins instantaneously as indicated by the transport model. This results in absorption of the latent heat of vaporization to facilitate the phase change. However, unlike boiling heat transfer, where heat is continuously supplied through an external heat source, the heat transfer in cavitating flow largely stems from the convective and conductive heat

DOI: 10.1002/fld

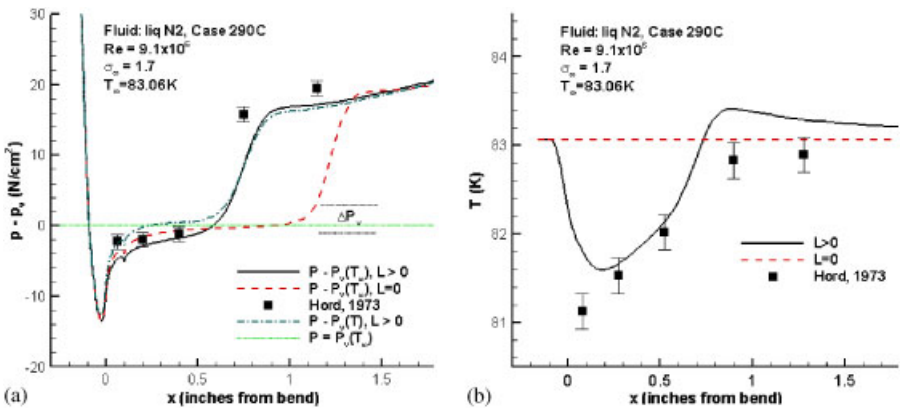

Figure 13. (a) Surface pressure and (b) surface temperature profile on 2D hydrofoil for Case 290C where the cavitation is controlled by (i) temperature-dependent vapor pressure (designated as $L>0$) and (ii) zero latent heat and hence isothermal flow field (designated as $L=0$). The range indicated by Δp_v shows the level of variations in vapor pressure caused by the temperature variations inside the cavity. (We use best-compromise model parameters $C_{dest}=0.639$, $C_{prod}=54.4$ to perform simulations.)

transfer, and the latent heat release/absorption within the fluid, with external heat source playing minor roles. Consequently, a decrease in fluid temperature is observed in the cavity region. As we approach the cavity closure region, the condensation of fluid releases latent heat increasing the fluid temperature locally. Furthermore, since the condensation process is dictated by the vapor pressure (with the local temperature effect exerted indirectly via the change in vapor pressure in response to the temperature field), the rate of latent heat release can be fast in comparison with the rate of convective and conductive heat transfer; consequently, in simulations, we observe an 'overshoot' in temperature profile. The experiments also show an increase in temperature of the fluid in the closure region, but probably due to the lack of sufficient number of probes on the surface, the existence of the overshoot could not be ascertained.

Overall, the pressure predictions on the hydrofoil surface follow the same trends as observed in experiments. However, we note differences in predictions with experimental data near the closure region of the cavity.

4.2. Impact of boundary conditions

To investigate the discrepancy between experimental and predicted surface pressure and temperature profiles, we also evaluate the impact of different thermal boundary conditions on the predictions. Although all the walls on the wind tunnel are modeled as adiabatic, the hydrofoil surface is modeled as either adiabatic (Neumann boundary) or specified temperature (Dirichlet boundary) wall. The temperature profile required for implementing Dirichlet boundary condition is obtained by inter-/extrapolating the experimental temperature at five probe locations on the surface of the hydrofoil.

The predicted pressure and temperature profiles on the surface of the hydrofoil obtained with different thermal boundary conditions are compared with the experimental data [35] in Figure 14. The introduction of heat transfer through the hydrofoil surface by Dirichlet boundary condition has little influence on the pressure distribution. With the given Reynolds number, the heat transfer at

DOI: 10.1002/fld

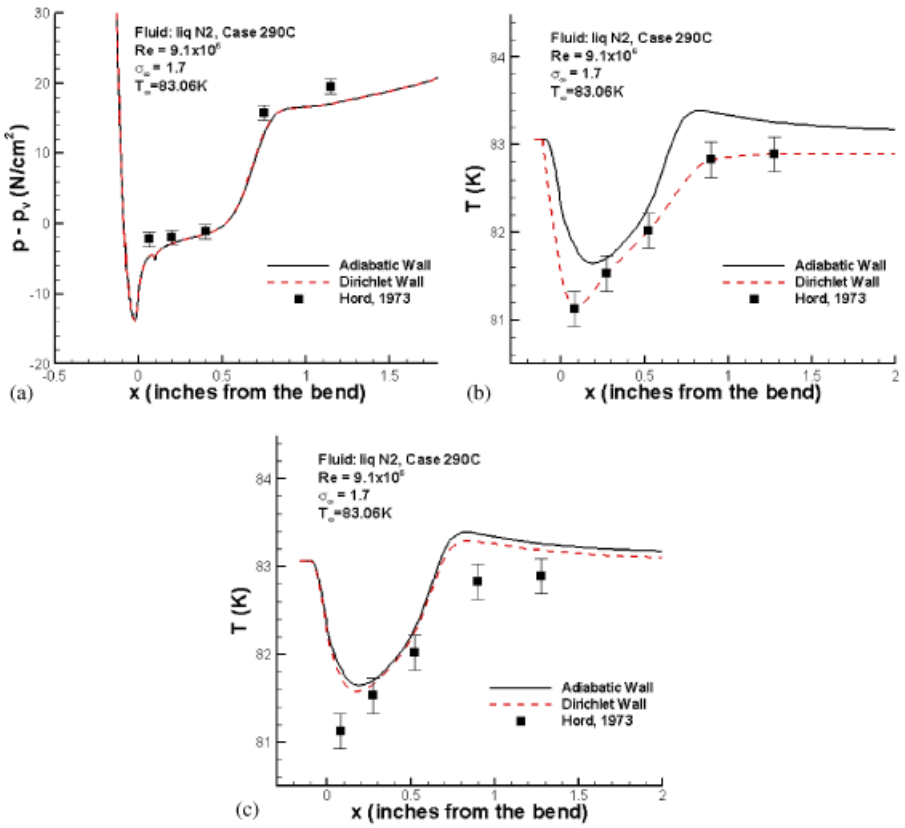

Figure 14. Impact of different boundary conditions on (a) surface pressure and (b) surface temperature profile on 2D hydrofoil (Case 290C, liquid N_2) and predictions on (c) first computational point next to boundary. We use best-compromise model parameters $C_{\text{dest}} = 0.639$, $C_{\text{prod}} = 54.4$ for simulations.

the hydrofoil surface is relatively small compared with the impact of latent heat; subsequently, only minor variations in the vapor pressures are observed. In the cavity closure region, the latent heat released during condensation cannot be redistributed via convection and conduction fast enough, resulting in an overshoot in temperature there. The temperature profile on the first computation point above the hydrofoil surface, shown in Figure 14(c), also indicates that the effect of heat transfer due to Dirichlet boundary condition is largely restricted to the boundary and has minimal influence on the flow inside the cavity.

Overall, it can be said that the effect of thermal boundary condition on the hydrofoil surface has little impact on the performance of the present cryogenic cavitation model.

5. CONCLUSIONS AND FUTURE WORK

In this paper, we presented results of model validation and improvement in a transport-based cryogenic cavitation model using benchmark experimental data for 2D hydrofoils provided by

DOI: 10.1002/fld

Hord [34, 35]. We used surrogate-based GSA to study the role of model parameters and uncertainties in temperature-dependent material properties. The model parameters originally used in present transport-based cavitation model [14] were calibrated for cryogenic environment using multiple surrogates and optimization techniques. The main conclusions of this paper are as follows:

(i) The performance of the current cryogenic cavitation model was affected more by model parameter associated with the evaporation source term (C_{dest}) than uncertainty in material properties. The high sensitivity index associated with temperature-dependent vapor density indicated significant impact on the accuracy of pressure and temperature predictions. The variations in the latent heat of vaporization influenced the accuracy of temperature predictions only. The model parameter associated with the production source term in the present cryogenic cavitation model C_{prod} did not influence predictions.

(ii) The best-compromise model parameters selected for present transport-based cavitation model [14] were $C_{\text{dest,LN}_2} = 0.639$, $C_{\text{dest,LH}_2} = 0.767$, and $C_{\text{prod}} = 54.4$. The choice of these parameters reduced the importance of evaporation source term, which resulted in the earlier onset of the condensation and hence the cavity closure. Utturkar *et al.* [25] have made adjustment based on trial and error ($C_{\text{dest,LN}_2} = 0.68$, $C_{\text{dest,LH}_2} = 0.816$, and $C_{\text{prod}} = 54.4$) and a limited optimization effort. In their approach, there was a lack of probing with regard to the sensitivity and robustness of the outcome. The merits of the present effort lie in a systematic use of the optimization and sensitivity methodology, a detailed assessment of the thermal boundary condition, and a reasonably broad range of fluid and flow cases.

(iii) Simultaneous use of multiple surrogate models evidently helped in increasing confidence in the results of GSA and optimization. The predictions using PWS model were more accurate than those using individual surrogate models.

(iv) The impact of thermal boundary conditions on the prediction of flow was apparently not significant. However, the thermal effect caused by the phase change (latent heat) clearly affects the cavitation dynamics, including the vapor pressure and, consequently, the cavity size. As we have shown here, the thermal effects play a very significant role in the accurate prediction of the pressure via phase change and thermo-sensitive material properties in cryogenic environment, with little impact caused by wall heat transfer.

(v) The trends of the optimization on pressure and thermal fields follow opposite directions. Although this indicates the usefulness of adopting a multi-objective optimization framework, as has been conducted here, it should also be pointed out again that in terms of practical impact, the pressure prediction is our primary objective because pressure fluctuation is what causes poor performance or even catastrophic situation in fluid machinery.

Although advancements in the pressure prediction capabilities of the present cavitation model have been made in this work, further model development at a conceptual level should be pursued to better address the discrepancies between measurements and computations, especially in the thermal field. We also acknowledge the need to further extend the current results to unsteady and/or super-cavitating flows that might require modifications in the cryogenic cavitation models. Finally, we note the lack of experimental data required to validate the detailed flow structures for cryogenic cavitating flows. We hope that more cryogenic cavitation experimental investigations would be carried out to offer insights into the flow fields.

DOI: 10.1002/fld

APPENDIX A: INFLUENCE OF TURBULENCE MODELING ON PREDICTIONS

We compare the influence of turbulence modeling on the predictions with the help of two benchmark cases of flow over a hydrofoil with liquid nitrogen (Case 290C) and liquid hydrogen (Case 249D). We compare the performance of the standard k–ε two-equation turbulence model [54] with the non-equilibrium k–ε turbulence model [55]. While the governing equations for the two models are the same (Equations (19)–(22)), the model constants are given in Table A1. We use $\beta_1 = 0.9$ and $\beta_2 = 1.15$.

The predicted surface pressure and temperature for the two test cases, shown in Figure A1, clearly demonstrate only moderate influence of turbulence models on the predictions.

Table A1. Model parameters in Launder–Spalding and non-equilibrium k–ε turbulence models.

Model	C_μ	C_{ε_1}	C_{ε_2}	σ_k	σ_ε
Standard k–ε [54]	0.09	1.44	1.92	1.0	1.3
Non-equilibrium k–ε model [55]	0.09	$\beta_1+(1.4-\beta_1)(P_t/\varepsilon)$	$\beta_2+(1.9-\beta_2)(P_t/\varepsilon)$	0.8927	1.15

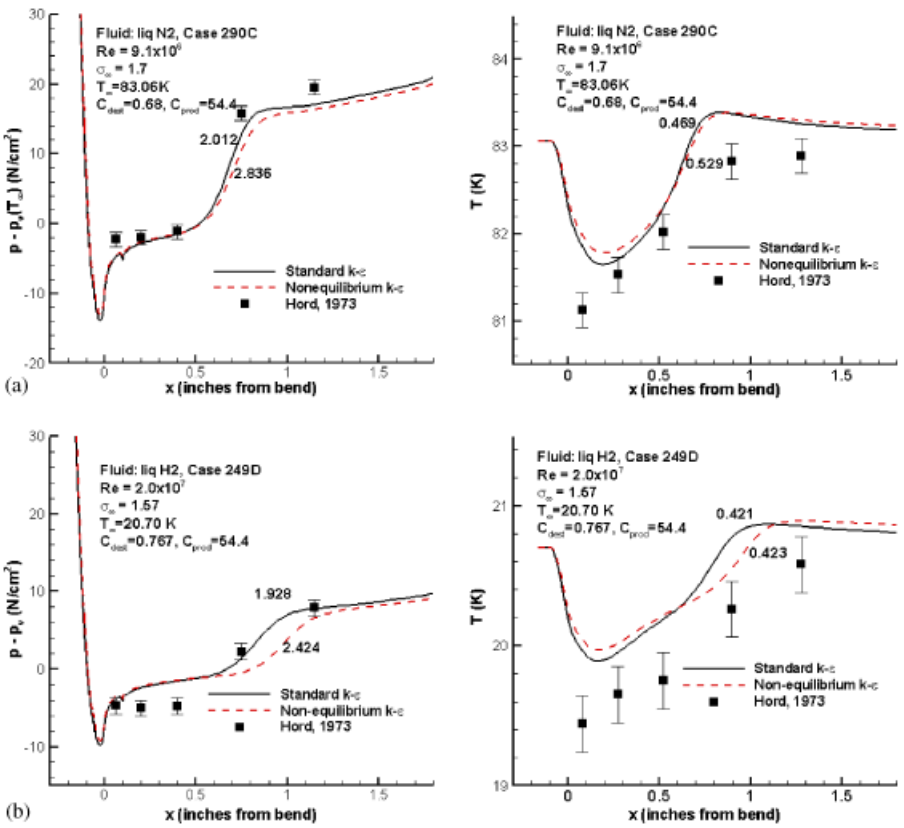

Figure A1. Influence of turbulence modeling on predictions in cryogenic cavitating conditions: surface and temperature plots for (a) Case 290C (liquid N_2, hydrofoil) and (b) Case 249D (liquid H_2, hydrofoil).

DOI: 10.1002/fld

APPENDIX B: GLOBAL SENSITIVITY ANALYSIS [50]

GSA was first presented by Sobol [50] in 1993. This method is used to estimate the effect of different variables on the total variability of the function. Some of the advantages of conducting a GSA include (i) assessing importance of the variables, (ii) fixing non-essential variables (which do not affect the variability of the function), thus reducing the problem dimensionality, etc. The theoretical formulation of the GSA is given as follows:

A function $f(\mathbf{x})$ of a square integrable objective as a function of a vector of independent uniformly distributed random input variables, $\mathbf{x}$ in domain $[0, 1]$, is assumed. This function can be decomposed into the sum of functions of increasing dimensionality as

$$f(\mathbf{x}) = f_0 + \sum_i f_i(x_i) + \sum_{i<j} f_{ij}(x_i, x_j) + \cdots + f_{12\cdots N_\mathrm{v}}(x_1, x_2, \ldots, x_{N_\mathrm{v}}) \tag{B1}$$

where $f_0 = \int_{\mathbf{x}=\mathbf{0}}^{\mathbf{1}} f \, \mathrm{d}\mathbf{x}$. If the following condition

$$\int_0^1 f_{i_1\cdots i_\mathrm{s}} \, \mathrm{d}x_k = 0 \tag{B2}$$

is imposed for $k = i_1, \ldots, i_\mathrm{s}$, then the decomposition described in Equation (B1) is unique. In the context of GSA, the total variance denoted as $V(f)$ can be shown to be equal to

$$V(f) = \sum_{i=1}^{N_\mathrm{v}} V_i + \sum_{1 \leqslant i,j \leqslant N_\mathrm{v}} V_{ij} + \cdots + V_{1\ldots N_\mathrm{v}} \tag{B3}$$

where $V(f) = E((f - f_0)^2)$ and each of the terms in Equation (B3) represents the partial contribution or partial variance of the independent variables (V_i) or set of variables to the total variance and provides an indication of their relative importance. The partial variances can be calculated using the following expressions:

$$\begin{aligned} V_i &= V(E[f|x_i]) \\ V_{ij} &= V(E[f|x_i, x_j]) - V_i - V_j \\ V_{ijk} &= V(E[f|x_i, x_j, x_j]) - V_{ij} - V_{ik} - V_{jk} - V_i - V_j - V_k \end{aligned} \tag{B4}$$

and so on, where V and E denote variance and expected value, respectively. Note that $E[f|x_i] = \int_0^1 f_i \, \mathrm{d}x_i$ and $V(E[f|x_i]) = \int_0^1 f_i^2 \, \mathrm{d}x_i$. Now, the sensitivity indices can be computed corresponding to the independent variables and set of variables. For example, the first- and second-order sensitivity indices can be computed as

$$S_i = \frac{V_i}{V(f)}, \quad S_{ij} = \frac{V_{ij}}{V(f)} \tag{B5}$$

Under the independent model inputs assumption, the sum of all the sensitivity indices is equal to one.

The first-order sensitivity index for a given variable represents the main effect of the variable but it does not take into account the effect of interaction of the variables. The total contribution

DOI: 10.1002/fld

of a variable on the total variance is given as the sum of all the interactions and the main effect of the variable. The total sensitivity index of a variable is then defined as

$$S_i^{\text{total}} = \frac{V_i + \sum_{j,j\neq i} V_{ij} + \sum_{j,j\neq i}\sum_{k,k\neq i} V_{ijk} + \cdots}{V(f)} \tag{B6}$$

Note that the above-referenced expressions can be easily evaluated using surrogate models of the objective functions. Sobol [50] has proposed a variance-based non-parametric approach to estimate the global sensitivity for any combination of design variables using Monte Carlo methods. To calculate the total sensitivity of any design variable x_i, the design variable set is divided into two complementary subsets of x_i and $Z(Z = x_j, \forall j = 1, N_v;\ j \neq i)$. The purpose of using these subsets is to isolate the influence of x_i from the influence of the remaining design variables included in Z. The total sensitivity index for x_i is then defined as

$$S_i^{\text{total}} = V_i^{\text{total}} / V(f) \tag{B7}$$

where

$$V_i^{\text{total}} = V_i + V_{i,Z} \tag{B8}$$

V_i is the partial variance of the objective with respect to x_i and $V_{i,Z}$ is the measure of the objective variance that is dependent on interactions between x_i and Z. Similarly, the partial variance for Z can be defined as V_z. Therefore, the total objective variability can be expressed as

$$V = V_i + V_Z + V_{i,Z} \tag{B9}$$

While Sobol [50] had used Monte Carlo simulations to conduct the GSA, the expressions given above can be easily computed analytically once the response surface model is available.

APPENDIX C: SURROGATE MODELING

Surrogate models are developed as a computationally inexpensive method to evaluate design objectives. There are many surrogate models, e.g. PRS approximations, KRG, RBNN, support vector regression, etc. A detailed discussion of different aspects of surrogate modeling was reviewed by Queipo *et al.* [7] and Li and Padula [8]. We give a brief description of different surrogate models here.

C.1. PRS approximation [66]

The observed response $y(\mathbf{x})$ of a function at point $\mathbf{x}$ is represented as a linear combination of basis functions $f_i(\mathbf{x})$ (mostly monomials are selected as basis functions) and coefficients β_i. Error in approximation ε is assumed to be uncorrelated and normally distributed with zero mean and σ^2 variance. That is,

$$y(\mathbf{x}) = \sum_i \beta_i f_i(\mathbf{x}) + \varepsilon, \quad E(\varepsilon) = 0, \quad V(\varepsilon) = \sigma^2 \tag{C1}$$

The PRS approximation of $y(\mathbf{x})$ is

$$\hat{y}(\mathbf{x}) = \sum_i b_i f_i(\mathbf{x}) \tag{C2}$$

DOI: 10.1002/fld

where b_i is the estimated value of the coefficient associated with the ith basis function $f_i(\mathbf{x})$. The coefficient vector $\mathbf{b}$ is obtained by minimizing the error in approximation ($e(\mathbf{x}) = y(\mathbf{x}) - \hat{y}(\mathbf{x})$) at N_s sampled design points in a least-square sense as

$$\mathbf{b} = (X^T X)^{-1} X^T \mathbf{y} \tag{C3}$$

where X is the matrix of basis functions and $\mathbf{y}$ is the vector of responses at N_s design points. The quality of approximation is measured by computing the coefficient of multiple determination R^2_{adj} and is defined as

$$R^2_{adj} = \frac{1 - \sigma_a^2 (N_s - 1)}{\sum_{i=1}^{N_s} (y_i - \overline{y})^2} \tag{C4}$$

where $\overline{y} = \sum_{i=1}^{N_s} / N_s$ and adjusted RMS error at sampling points is given as $\sigma_a = \sqrt{\sum_{i=1}^{N_s} (y(\mathbf{x}_i) - \hat{y}(\mathbf{x}_i))^2 / (N_s - N_\beta)}$. For a good fit, R^2_{adj} should be close to 1. For more details on PRS approximation, refer to Myers and Montgomery [66].

C.2. Kriging [67]

Kriging is named after the pioneering work of D. G. Krige (a South African mining engineer). KRG estimates the value of an objective function $y(\mathbf{x})$ at design point $\mathbf{x}$ as the sum of a linear polynomial trend model $\sum_{i=1}^{N_v} \beta_i f_i(\mathbf{x})$ and a systematic departure $Z(\mathbf{x})$ representing low-frequency (large-scale) and high-frequency (small-scale) variations around the trend model

$$y(\mathbf{x}) = \hat{y}(\mathbf{x}) = \sum_i \beta_i f_i(\mathbf{x}) + Z(\mathbf{x}) \tag{C5}$$

The systematic departure components are assumed to be correlated as a function of distance between the locations under consideration. Gaussian function is the most commonly used correlation function

$$C(Z(\mathbf{x}), Z(\mathbf{s}), \boldsymbol{\theta}) = \prod_{i=1}^{N_v} \exp(-\theta_i (x_i - s_i)^2) \tag{C6}$$

The parameters β_i, θ_i are obtained using maximum likelihood estimates [68]. In this paper, we have used a linear trend model and a Gaussian correlation model to approximate all responses. The correlation parameters θ_i vary between $[0.1, 100]$.

C.3. Radial basis neural network [69]

The objective function is approximated as a weighted combination of responses from radial basis functions (also known as neurons)

$$\hat{y}(\mathbf{x}) = \sum_{i=1}^{N_{RBF}} w_i a_i(\mathbf{x}) \tag{C7}$$

where $a_i(\mathbf{x})$ is the response of the ith radial basis function at design point $\mathbf{x}$ and w_i is the weight associated with $a_i(\mathbf{x})$. Mostly Gaussian function is used for radial basis function $a(\mathbf{x})$ as

$$a = \text{radbas}(\|\mathbf{s} - \mathbf{x}\| b), \quad \text{radbas}(n) = e^{-n^2} \tag{C8}$$

DOI: 10.1002/fld

Parameter b in the above equation is inversely related to a user-defined parameter 'spread constant' that controls the response of the radial basis function. A higher spread constant would cause the response of neurons to be very smooth and very high spread constant would result into a highly non-linear response function. Typically, spread constant is selected between zero and one. The number of radial basis functions (neurons) and associated weights are determined by satisfying the user-defined error 'goal' on the mean square error in approximation. In this paper, the value of mean square error goal is taken as the square of 5% of the mean response at data points.

As discussed here, we have many surrogate models and it is unknown *a priori*, which surrogate would be most suitable for a given problem. Besides, the choice of best surrogate model changes with sampling density and nature of the problem [51]. It has been shown by Goel *et al.* [51] that in such a scenario simultaneously using multiple surrogate models protects us from choosing wrong surrogates. They proposed using a weighted averaged surrogate that is described as follows.

C.4. PRESS-based weighted average surrogate model [*51*]

We develop a weighted average surrogate model as

$$\hat{y}_{\mathrm{pws}}(\mathbf{x}) = \sum_{i}^{N_{\mathrm{SM}}} w_i \hat{y}_i(\mathbf{x}) \tag{C9}$$

where $\hat{y}_{\mathrm{pws}}(\mathbf{x})$ is the predicted response by the weighted average of surrogate models, $\hat{y}_i(\mathbf{x})$ is the predicted response by the ith surrogate model, and w_i is the weight associated with the ith surrogate model at design point $\mathbf{x}$. Furthermore, the sum of the weights must be one ($\sum_{i=1}^{N_{\mathrm{SM}}} w_i = 1$) so that if all the surrogates agree, $\hat{y}_{\mathrm{pws}}(\mathbf{x})$ will also be the same. Weights are determined as follows:

$$\begin{gathered} w_i^* = (E_i + \alpha E_{\mathrm{avg}})^{\beta}, \quad w_i = \frac{w_i^*}{\sum_i w_i^*} \\ E_{\mathrm{avg}} = \frac{\sum_{i=1}^{N_{\mathrm{SM}}} E_i}{N_{\mathrm{SM}}}, \quad \beta < 0, \ \ \alpha < 1 \end{gathered} \tag{C10}$$

where E_i is the global data-based error measure for ith surrogate model. In this study, generalized mean square cross-validation error (GMSE) (leave-one-out cross validation or PRESS in PRS approximation terminology), defined in Appendix C, is used as global data-based error measure, by replacing E_i by $\sqrt{\mathrm{GMSE}_i}$. We use $\alpha = 0.05$ and $\beta = -1$ in this paper. The above-mentioned formulation of weighting schemes is used with PRS approximation, KRG, and RBNN such that

$$\hat{y}_{\mathrm{pws}} = w_{\mathrm{prs}} \hat{y}_{\mathrm{prs}} + w_{\mathrm{krg}} \hat{y}_{\mathrm{krg}} + w_{\mathrm{rbnn}} \hat{y}_{\mathrm{rbnn}} \tag{C11}$$

For more details about the weighted average surrogate model, we refer the reader to Goel *et al.* [51].

APPENDIX D: GENERALIZED MEAN SQUARE CROSS-VALIDATION ERROR (GMSE OR PRESS)

In general, the data are divided into k subsets (k-fold cross-validation) of approximately equal size. A surrogate model is constructed k times, each time leaving out one of the subsets from

DOI: 10.1002/fld

training and using the omitted subset to compute the error measure of interest. The generalization error estimate is computed using the k error measures obtained (e.g. average). If k equals the sample size, this approach is called leave-one-out cross-validation (also known as PRESS in the PRS approximation terminology). The following equation represents a leave-one-out calculation when the generalization error is described by the mean square error (GMSE):

$$\mathrm{GMSE} = \frac{1}{k}\sum_{i=1}^{k}(y_i - \hat{y}_i^{(-i)})^2 \tag{D1}$$

where $\hat{y}_i^{(-i)}$ represents the prediction at $\mathbf{x}^{(i)}$ using the surrogate constructed using all sample points except $(\mathbf{x}^{(i)}, y_i)$. Analytical expressions are available for that case for the GMSE without actually performing the repeated construction of the surrogates for both PRS [66, Section 2.7] and KRG [70]; however, here we used brute-force. The advantage of cross-validation is that it provides nearly unbiased estimate of the generalization error and the corresponding variance is reduced (compared with split-sample) considering that every point gets to be in a test set once, and in a training set $k-1$ times (regardless of how the data are divided).

NOMENCLATURE

$\mathbf{b}$	estimated coefficient vector associated with polynomial basis functions
$C_{\mathrm{dest}}, C_{\mathrm{prod}}$	empirical parameters used in cavitation model
C_p	specific heat
$C_{\varepsilon_1}, C_{\varepsilon_2}$	k–ε turbulence model coefficients
D	characteristic length scale
$E(f(x))$	expected value of $f(x)$ with respect to x
$f(\mathbf{x})$	function of variable vector $\mathbf{x}$
f_{v}	mass fraction of vapor
h	specific enthalpy
k	turbulent kinetic energy
K	thermal conductivity
L	latent heat of vaporization
$\dot{m}^-, \dot{m}^+$	cavitation source terms
$\min(a, b)$	minimum of a and b
$\max(a, b)$	maximum of a and b
N_{RBF}	number of radial basis functions
N_{s}	number of sampled points
N_{sm}	number of surrogate models
N_β	number of basis functions in polynomial response surface approximation
N_{var}	number of variables
p	pressure
P_{diff}	L_2 norm of difference between experimental and predicted pressures
P_{t}	production term in turbulence model
p_{v}	vapor pressure
R	liquid to vapor density ratio
R^2_{adj}	adjusted coefficient of determination

DOI: 10.1002/fld

RMSE	root mean square error
S	sensitivity index
S_i	sensitivity index of main effects (x_i)
S_{iz}	sensitivity index of variable x_i with other variables
S_i^{total}	total sensitivity index of variable x_i
t	time
t_∞	reference time scale
T	temperature
T_{diff}	L_2 norm of difference between experimental and predicted temperatures
u	velocity
U_∞	reference velocity scale
V	total variance of a function $f(\mathbf{x})$
V_i	partial variance of $f(\mathbf{x})$ with respect to x_i (main effects)
$V_{i,Z}$	partial variance of $f(\mathbf{x})$ with respect to interactions of x_i (interaction effects)
V_i^{total}	total variance of $f(\mathbf{x})$ with respect to x_i
w_i	weight associated with ith surrogate model
x	space variable
$\mathbf{x}$	vector of variables
X	design matrix
$y(\mathbf{x})$	actual response at point $\mathbf{x}$
$\hat{y}(\mathbf{x})$	predicted response at point $\mathbf{x}$
$Z(\mathbf{x})$	systematic departure in kriging
α	liquid volume fraction
α, β	parameters associated with weighted average surrogate
$\boldsymbol{\beta}$	true coefficient vector associated with polynomial basis functions
ε	turbulent dissipation term, noise in surrogate models
$\boldsymbol{\theta}$	vector of parameters associated with the Gaussian correlation function
μ	dynamic viscosity
ρ	density
σ	cavitation number, estimated standard deviation of noise
$\sigma_\varepsilon, \sigma_k$	k–ε turbulence model coefficients
ϕ	mixture property

Acronyms

CFD	computational fluid dynamics
CVS	controlled variation scheme
FCCD	face-centered cubic composite design
GMSE	generalized mean square (cross-validation) error
KRG	kriging
LH_2	liquid hydrogen
LHS	latin hypercube sampling
LN_2	liquid nitrogen
LO_X	liquid oxygen
POF	pareto optimal front
PRESS	square root of predicted residual sum of squares
PRS	polynomial response surface approximation

DOI: 10.1002/fld

RBNN	radial basis neural network
PWS	PRESS-based weighted average surrogate

Subscripts

baseline	baseline parameters
c	cavity
l	liquid
m	mixture
KRG	quantity associated with Kriging
PRS	quantity associated with polynomial response surface
RBNN	quantity associated with radial basis neural network
rms	root mean square of the quantity
t	turbulent
v	vapor
∞	free-stream quantities

Superscripts

$*$	scale factors and normalized quantities

ACKNOWLEDGEMENTS

The present efforts have been supported by the Institute for Future Space Transport, under the NASA Constellation University Institute Program (CUIP), Ms Claudia Meyer program monitor. This material is based on the work supported by the National Science Foundation under Grant No. 0423280. We acknowledge the valuable collaboration with Dr Yogen Utturkar and Dr Jiongynag Wu during their doctoral research and afterwards. We acknowledge the anonymous reviewers for their erudite comments and constructive criticism that immensely helped us improve the paper.

REFERENCES

1. Roache PJ, Ghia K, White F. Editorial policy statement on the control of numerical accuracy. *Journal of Fluids Engineering* (ASME) 1986; **108**(1):2.
2. AIAA. Editorial policy statement on numerical accuracy and experimental uncertainty. *AIAA Journal* 1994; **32**:3.
3. ASME Editorial Board. Journal of heat transfer editorial policy statement on numerical accuracy. *Journal of Heat Transfer* (ASME) 1994; **116**:797–798.
4. AIAA. Guide for the verification and validation of computational fluid dynamics simulations. *AIAA G-077-1998*, 1998.
5. Roache PJ. *Verification and Validation in Computational Science and Engineering*. Hermosa Publishers: Albuquerque, NM, 1998.
6. Oberkampf WL, Trucano TG, Hirsch C. Verification, validation, and predictive capability in computational engineering and physics. *Applied Mechanics Review* 2004; **57**(5):345–384.
7. Queipo NV, Haftka RT, Shyy W, Goel T, Vaidyanathan R, Tucker PK. Surrogate based analysis and optimization. *Progress in Aerospace Sciences* 2005; **41**(1):1–28.
8. Li W, Padula S. Approximation methods for conceptual design of complex systems. In *Proceedings of 11th International Conference on Approximation Theory*, Chui C, Neaumtu M, Schumaker L (eds). Gatlinburg, TN, May 2004.
9. Batchelor GK. *An Introduction to Fluid Dynamics*. Cambridge University Press: Cambridge, 1967.
10. Brennen CE. *Hydrodynamics of Pumps*. Oxford University Press: Oxford, 1994.
11. Brennen CE. *Cavitation and Bubble Dynamics*. Oxford University Press: Oxford, 1995.
12. NASA online facts. http://www-pao.ksc.nasa.gov/kscpao/nasafact/count2.htm, 1991.

DOI: 10.1002/fld

13. Garcia R. NASA Marshall Space Flight Center, Personal Communications, 2001.
14. Merkle CL, Feng J, Buelow PEO. Computational modeling of dynamics of sheet cavitation. *Proceedings of 3rd International Symposium on Cavitation*, Grenoble, France, 1998.
15. Ahuja V, Hosangadi A, Arunajatesan S. Simulations of cavitating flows using hybrid unstructured meshes. *Journal of Fluids Engineering* 2001; **123**(2):331–340.
16. Venkateswaran S, Lindau JW, Kunz RF, Merkle CL. Computation of multiphase mixture flows with compressibility effects. *Journal of Computational Physics* 2002; **180**(1):54–77.
17. Kunz RF, Boger DA, Stinebring DR, Chyczewski TS, Lindau JW, Gibeling HJ. A preconditioned Navier–Stokes method for two-phase flows with application to cavitation. *Computers and Fluids* 2000; **29**(8):849–875.
18. Athavale MM, Singhal AK. Numerical analysis of cavitating flows in rocket turbopump elements. *Proceedings of 37th AIAA/ASME/SAE/ASEE Joint Propulsion Conference and Exhibit*, Salt Lake City, UT, 8–11 July 2001; AIAA Paper 2001-3400.
19. Senocak I, Shyy W. A pressure-based method for turbulent cavitating flow computations. *Journal of Computational Physics* 2002; **176**:363–383.
20. Senocak I, Shyy W. Interfacial dynamics-based modeling of turbulent cavitating flows. Part-1: Model development and steady-state computations. *International Journal for Numerical Methods in Fluids* 2004; **44**(9):975–995.
21. Senocak I, Shyy W. Interfacial dynamics-based modeling of turbulent cavitating flows. Part-2: Time-dependant computations. *International Journal for Numerical Methods in Fluids* 2004; **44**(9):997–1016.
22. Kubota A, Kato H, Yamaguchi H. A new modeling of cavitating flows: a numerical study of unsteady cavitation on a hydrofoil section. *Journal of Fluid Mechanics* 1992; **240**:59–96.
23. Edwards JR, Franklin RK, Liou MS. Low-diffusion flux splitting methods for real fluid flows with phase transitions. *AIAA Journal* 2000; **38**(9):1624–1633.
24. Ventikos Y, Tzabiras G. A numerical method for simulation of steady and unsteady cavitating flows. *Computers and Fluids* 2000; **29**(1):63–88.
25. Utturkar Y, Thakur SS, Shyy W. Computational modeling of thermodynamic effects in cryogenic cavitation. *Proceedings of 43rd AIAA Aerospace Sciences Meeting and Exhibit*, Reno, NV, January 2005; AIAA Paper 2005-1286.
26. Wang G, Senocak I, Shyy W, Ikohagi T, Cao S. Dynamics of attached turbulent cavitating flows. *Progress in Aerospace Sciences* 2001; **37**(6):551–581.
27. Preston A, Colonius T, Brennen CE. Towards efficient computation of heat and mass transfer effects in the continuum model for bubbly cavitating flows. *Proceedings of the 4th International Symposium on Cavitation*, Pasadena, CA, 2001.
28. Utturkar Y, Wu J, Wang G, Shyy W. Recent progress in modeling of cryogenic cavitation for liquid rocket propulsion. *Progress in Aerospace Sciences* 2005; **41**(7):558–608.
29. Utturkar Y. Computational modeling of thermodynamic effects in cryogenic cavitation. *Ph.D. Dissertation*, University of Florida, Gainesville, FL, 2005.
30. Hosangadi A, Ahuja V. Numerical study of cavitation in cryogenic fluids. *Journal of Fluids Engineering* 2005; **127**(2):267–281.
31. Lemmon EW, McLinden MO, Huber ML. *REFPROP*: *Reference Fluid Thermodynamic and Transport Properties*, *NIST Standard Database 23*, National Institute of Standards and Technology (NIST), version 7.0, 2002.
32. Stahl HA, Stepanoff AJ. Thermodynamic aspects of cavitation in centrifugal pumps. *Transactions of ASME* 1956; **78**:1691–1693.
33. Gelder TF, Ruggeri RS, Moore RD. Cavitation similarity considerations based on measured pressure and temperature depressions in cavitated regions of Freon-114. *NASA Technical Note D-3509*, 1966.
34. Ruggeri RS, Moore RD. Method of prediction of pump cavitation performance for various liquids, liquid temperatures and rotation speeds. *NASA Technical Note D-5292*, 1969.
35. Hord J. Cavitation in liquid cryogens, II—Hydrofoil. *NASA CR-2156*, 1973.
36. Holl JW, Billet ML, Weir DS. Thermodynamic effects on developed cavitation. *Journal of Fluids Engineering* 1975; **97**(4):507–516.
37. Cooper P. Analysis of single and two-phase flows in turbopump inducers. *Journal of Engineering Power* (ASME) 1967; **89**:577–588.
38. Franc JP, Rebattet C, Coulon A. An experimental investigation of thermal effects in a cavitating inducer. *Proceedings of Fifth International Symposium on Cavitation*, Osaka, Japan, 2003.
39. Hord J. Cavitation in liquid cryogens, III—Ogives. *NASA CR-2242*, 1973.

DOI: 10.1002/fld

40. Hosangadi A, Ahuja V. A generalized multi-phase framework for modeling cavitation in cryogenic fluids. *Proceedings of 33rd AIAA Fluid Dynamics Conference and Exhibit*, Orlando, FL, June 2003; AIAA Paper 2003-4000.
41. Reboud JL, Sauvage-Boutar E, Desclaux J. Partial cavitation model for cryogenic fluids. *Proceedings of Cavitation and Multiphase Flow Forum*, Toronto, Canada, 1990.
42. Delannoy Y, Reboud JL. Heat and mass transfer on a vapor cavity. *Proceedings of ASME Fluids Engineering Conference*, vol. 165, Washington, DC, 1993; 209–214.
43. Deshpande M, Feng J, Merkle CL. Numerical modeling of the thermodynamic effects of cavitation. *Journal of Fluids Engineering* 1997; **119**(2):420–427.
44. Lertnuwat B, Sugiyama K, Matsumoto Y. Modeling of thermal behavior inside a bubble. *Proceedings of Fourth International Symposium on Cavitation*, Pasadena, CA, 2001.
45. Tokumasu T, Kamijo K, Matsumoto Y. A numerical study of thermodynamic effects of sheet cavitation. *Proceedings of ASME FEDSM'02*, Montreal, Canada, 2002.
46. Tokumasu T, Sekino Y, Kamijo K. A new modeling of sheet cavitation considering the thermodynamic effects. *Proceedings of 5th International Symposium on Cavitation*, Osaka, Japan, 2003.
47. Hosangadi A, Ahuja V, Ungewitter RJ. Generalized numerical framework for cavitation in inducers. *Proceedings of 2003 ASME/JSME Joint Fluids Engineering Conference*, Honolulu, HI, July 2003; ASME Paper FEDSM2003-45408.
48. Rachid FBF. A thermodynamically consistent model for cavitating flows of compressible fluids. *International Journal of Non-linear Mechanics* 2003; **38**:1007–1018.
49. Rapposelli E, Agostino LD. A barotropic cavitation model with thermodynamic effects. *Proceedings of Fifth International Symposium on Cavitation*, Osaka, Japan, 2003.
50. Sobol IM. Sensitivity analysis for nonlinear mathematical models. *Mathematical Modeling and Computational Experiment* 1993; **1**(4):407–414.
51. Goel T, Haftka RT, Shyy W, Queipo NV. Ensemble of multiple surrogates. *Structural and Multidisciplinary Optimization* 2007; **33**(3):199–216.
52. Goel T, Vaidyanathan R, Haftka RT, Shyy W, Queipo NV, Tucker PK. Response surface approximation of Pareto optimal front in multi-objective optimization. *Computer Methods in Applied Mechanics and Engineering* 2007; **196**(4–6):879–893.
53. Wu J, Utturkar Y, Senocak I, Shyy W, Arakere N. Impact of turbulence and compressibility modeling on three-dimensional cavitating flow computations. *Proceedings of 33rd AIAA Fluid Dynamics Conference and Exhibit*, Orlando, FL, June 2003; AIAA Paper 2003-4264.
54. Launder BE, Spalding DB. The numerical computation of turbulent flows. *Computer Methods in Applied Mechanics and Engineering* 1974; **3**:269–289.
55. Shyy W, Thakur SS, Ouyang H, Liu J, Blosch E. *Computational Techniques for Complex Transport Phenomenon*. Cambridge University Press: Cambridge, U.K., 1997.
56. Wu J, Wang G, Shyy W. Time-dependent turbulent cavitating flow computations with interfacial transport and filter-based models. *International Journal of Numerical Methods in Fluids* 2005; **49**(7):739–761.
57. Vaidyanathan R, Senocak I, Wu J, Shyy W. Sensitivity evaluation of a transport-based turbulent cavitation model. *Journal of Fluids Engineering* 2003; **125**(3):447–458.
58. Thakur SS, Wright J, Shyy W. STREAM: a computational fluid dynamics and heat transfer Navier–Stokes solver. Theory and applications. *Technical Report*, Streamline Numerics, Inc. and Computational Thermo-Fluids Laboratory, Department of Mechanical and Aerospace Engineering, Gainesville, FL, 2002.
59. Shyy W, Sun C-S. Development of a pressure-correction/staggered-grid based multigrid solver for incompressible recirculating flows. *Computers and Fluids* 1993; **22**:51–76.
60. Shyy W, Thakur SS. A controlled variation scheme in a sequential solver for recirculating flows. Part-I: Theory and formulation. *Numerical Heat Transfer B-Fundamentals* 1994; **25**(3):245–272.
61. Shyy W. A study of finite difference approximations to steady-state, convection-dominated flow problems. *Journal of Computational Physics* 1985; **57**:415–438.
62. Versteeg HK, Malalasekera W. *An Introduction to Computational Fluid Dynamics*: *The Finite Volume Method*. Pearson Education Limited: England, 1995.
63. Abramowitz M, Stegun IA (eds). Integration. *Handbook of Mathematical Functions with Formulas*, *Graphs*, *and Mathematical Tables*, Section 25.4. Dover: New York, 1972; 885–887.
64. Miettinen KM. *Nonlinear Multiobjective Optimization*. Kluwer Academic Publishers: Boston, 1999.
65. Chankong V, Haimes YY. *Multi-objective Decision Making Theory and Methodology*. Elsevier: New York, 1983.

DOI: 10.1002/fld

66. Myers RH, Montgomery DC. *Response Surface Methodology*. Wiley: New York, 1995.
67. Matheron G. Principles of geostatistics. *Economic Geology* 1963; **58**:1246–1266.
68. Lophaven SN, Nielsen HB, Sondergaard J. *DACE*: *A Matlab Kriging Toolbox*, *Version 2.0*. Information and Mathematical Modeling, Technical University of Denmark, 2002.
69. Orr MJL. *Introduction to Radial Basis Function Networks*. Center for Cognitive Science, Edinburg University, Scotland, U.K., 1996. http://www.anc.ed.ac.uk/∼mjo/rbf.html.
70. Martin JD, Simpson TW. Use of kriging models to approximate deterministic computer models. *AIAA Journal* 2005; **43**(4):853–863.

DOI: 10.1002/fld